TUTORIAL

Visible and near-infrared Fourier transform spectroscopy with a common-path interferometer

To cite this article: Antonio Perri 2021 *J. Phys. B: At. Mol. Opt. Phys.* **54** 113001

View the article online for updates and enhancements.

Visible and near-infrared Fourier transform spectroscopy with a common-path interferometer

Antonio Perri*

NIREOS s.r.l., Milano, Italy

E-mail: antonio.perri@nireos.com

CrossMark

Abstract

Optical spectrometers can be generally divided into two categories, frequency-domain and time-domain ones. The former includes compact, industrial-grade instruments that are easily available in the visible spectral range. The latter are lab-grade, bulky and fragile instruments that offer very high sensitivity and accuracy but are mainly limited to the infrared spectral region. This manuscript aims to present a time-domain device and several of its applications in which it is possible to combine some of the advantages of the two techniques, finally, bringing the advantage of Fourier transform spectroscopy down to the visible and near-infrared spectral regions. The device is a common-path interferometer based on birefringence. The concept is straightforward, and it is a compact, robust, and cost-effective instrument, and it has been applied in a wide range of applications. In this manuscript, the interferometer will be described from a theoretical point of view, and its capabilities will be presented applied to the measurement of fluorescence excitation–emission matrix maps down to the ultimate sensitivity at the single-molecule level, time-resolved photoluminescence spectra, spectral images, and the complex optical activity.

(Some figures may appear in colour only in the online journal)

1. Introduction

There are two ways to measure the light spectrum of an emitting source. The first one is the dispersive technique. The light is separated into its spectral components employing a grating or a prism. The intensity contribution of each component is measured either serially or in parallel by a multichannel detector array. The second one is the so-called time-domain approach, and it employs an interferometer to create two replicas of the incoming light retarded by a variable delay. A single-pixel detector measures the interference signal between the two light replicas as a function of the variable delay, and the spectrum is retrieved by performing a Fourier transform (FT) of the measured signal. The dispersive technique is widely used in the academic and industrial fields, especially in the visible spectral range, where multichannel detector arrays are not expensive due to their compactness and robustness.

However, the use of FT-approach carries several advantages with respect to dispersive technologies. All the wavelengths are measured simultaneously, thus increasing the number of photons reaching each pixel of the detector and decreasing measurement times. This leads to a higher signal-to-noise ratio when the detector noise is the predominant noise source (Fellgett's advantage) [1]. The etendue of an interferometer is much higher with respect to dispersive technologies leading to more light throughput and sensitivity (Jacquinot advantage) [2]. This is mainly due to an entrance slit whose width varies from tens to hundreds of micrometers, partially blocking the input radiation. Higher versatility since the interferometer's scan range changes the spectral

* Author to whom any correspondence should be addressed.

resolution without changing the instrument hardware. The throughput of the system, hence the instrument's sensitivity, does not change, increasing the spectral resolution. Interferometers are usually calibrated with known laser lines whose positions are known with great precision. Their measurements are accurate and reproducible. Thus a frequent calibration is not required, contrary to some other technologies (the Connes advantage).

However, in an ordinary double-beam interferometer, the two replicas are created employing a beam splitter, and they travel along different paths. This causes problems because it is challenging to maintain interferometric stability between the two different interferometer arms due to environmental vibrations and perturbations. Indeed, for this approach to work, the path length difference must not fluctuate more than $\frac{\lambda}{10}$, where λ is the radiation wavelength, and this is the main reason why this technique is de facto restricted to the infrared spectral region and cannot be easily used outside the laboratory environments. The interferometric stabilization of the interferometer is typically performed by a complicated and expensive feedback loop system, requiring a reference signal from a He–Ne laser, leading to costly and bulky instruments.

This manuscript aims to present a device and several applications in which it is possible to combine some of the advantages of the two techniques, finally, bringing the advantage of FT-spectroscopy down to the visible and near-infrared spectral regions leading to the development of a compact, robust and cost-effective instrument. The drawbacks of the double-beam interferometers were circumvented by developing and using a common-path interferometer (CPI). The two replicas are not geometrically divided into two paths in this device, but they travel into the same one. Therefore, the two replicas experience the same perturbations from the environment, keeping constant the relative delay between the two within a few attoseconds. The replicas are divided in polarization rather than spatially. They are delayed by exploiting the birefringence of a uniaxial crystal. This device does not require any active stabilization or He–Ne laser reference, leading to a compact instrument footprint. The device is insensitive to environmental vibrations, making it an industrial-grade device.

The CPI was used in several different applications, showing this kind of interferometer's potential as an enabling technology across several scientific fields. It was used as a simple spectrometer in the infrared spectral region [3]. Moreover, it was used in pump-probe spectroscopy [4, 5] and coherent Raman scattering as a broadband spectrometer working with high-frequency modulation [6, 7]. Following the same principle, a slightly modified version called TWINS comprising two additional birefringent crystals was used in ultrafast two-dimensional spectroscopy [8, 9]. It was recently employed as the key element in a photocurrent microscope [10] and quantum optics [11]. This manuscript focuses on several different applications, especially in the visible and near-infrared spectral region, where it is usually hard to apply FT-spectroscopy. As a starting point, the CPI will be presented as a tool for single-point spectroscopy. The system can be used to completely study the fluorescence properties of matter, extracting information related to the excitation, emission, and lifetime

properties of the sample. In detail, the CPI will be applied to the measurement of excitation–emission maps (EEM) down to the ultimate sensitivity limit at the single-molecule level, and to the measurement of time-resolved photo-luminescence (TRPL) spectra. For agricultural, pharmaceutical, and food industries chemical studies it is not sufficient to study the excitation and/or the emission spectrum of a sample. Indeed, since almost all biological molecules are chiral, it is often needed to characterize how the light polarization state rotates as it travels through a material of interest. This can be done by employing the CPI's sensitivity to the incoming light's polarization state. This feature will be discussed and applied to the measurement of chiral samples' chiro-optical activity, simultaneously measuring the circular dichroism and circular birefringence spectra. However, in these applications, we can only extract information about a single point of the sample. This is not enough to completely characterize the properties of a heterogenous sample. For this reason, the CPI capability will be presented extending the source from a single point to a wide field scene in measuring spectral images. This CPI-based spectral imager is very versatile and has been used in applications ranging from microscopy to remote sensing, hence from the microscopic to the macroscopic world.

2. The common path interferometer (CPI)

The interferometer used in all the experiments described in this manuscript is a common-path device based on birefringence, which belongs to polarization-division interferometers. The device comprises a Soleil–Babinet compensator, and it is turned into an interferometer by adding entrance and exit polarizers. This section describes the device in detail, focusing on the differences with respect to a Michelson's interferometer and their consequences as the need to perform a spectral and intensity calibration.

2.1. Constituent elements and working principles

Figure 1 shows a basic scheme of the CPI. The interferometer's first element is a polarizer having the transmission axis oriented at 45° with respect to the horizontal axis. After this element, the light is polarized alongside the transmission axis and can be considered the superposition of vertical and horizontal polarized components. The second element is a uniaxial birefringent block with the optical axis oriented transversely to the optical beam.

The optical axis of a uniaxial-birefringent crystal coincides with the extraordinary axis.

Therefore, the light passing into the block with a polarization parallel to this axis experiences a refractive index equal to the extraordinary one. Oppositely, the light having a polarization state perpendicular to this axis experiences an ordinary refractive index. Figure 2 shows the effect of this element. Since the two polarization components travel at a different speed inside the crystal, after the propagation, a fixed delay $\tau = \Delta n d/c$, where $\Delta n = n_{\mathrm{e}} - n_{\mathrm{o}}$ is the birefringence of the material, and c is the speed of light in vacuum, separates the two components. The final result is the generation
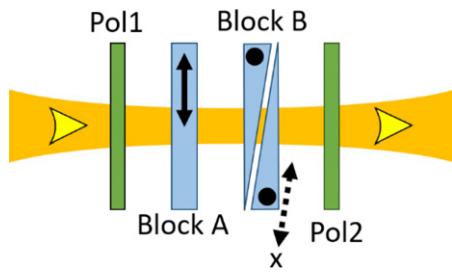
Figure 1. This figure shows a basic scheme of the CPI. The constituent blocks are an entrance and an exit polarizer oriented with their transmission axis at 45°, namely, Pol1 and Pol2; a first birefringent block (block A) and a second one (block B) composed of two wedges with the same apex angle. The arrow and the dots in block A and B highlight the optical axis of the crystals. The tilted-dashed arrow in the second wedge indicates the crystal's movement direction. This movement changes the effective thickness of block A.
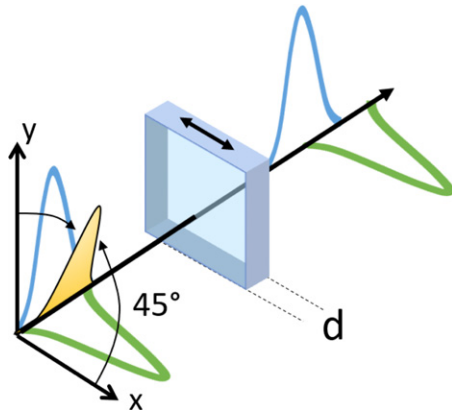

Figure 2. This figure shows what happens to the vertical and horizontal polarization components by passing through a birefringent block with thickness 'd'. The block's optical axis is indicated as a black arrow.

of two collinear and superimposed orthogonal replicas of the input radiation having a fixed relative delay. Please note that, for visualization purposes, figure 2 shows pulses of light, but the same description also works considering continuous-wave radiation.

In an interferometer, the relative delay can be tuned from a positive value to a negative one by physically changing the two replicas' path-length difference. For example, in a Michelson's interferometer, this is performed by moving a mirror in one arm of the interferometer. As indicated in figure 1, by inserting in the beam-path a birefringent block comprising a couple of birefringent wedges with the same apex angle α, we can reproduce the same behavior. Then, by varying the insertion of one of the two wedges through a motor, it is possible to tune the material's effective thickness, hence the relative delay between the two replicas. The motor is a precision linear stage, and the second wedge moves along a direction x in figure 1 with an angle of $90° - \alpha$ with respect to the light beam. This is necessary to keep the gap constant in between the two crystals while moving the second wedge.

Adding in series the first and the second birefringent elements, we can build the CPI. As shown in figure 1, the two blocks' optical axes are orthogonal to each other. In this way, we can vary the delay from positive to negative delay. Indeed, considering the position $x = 0$ to be the one corresponding to an equal thickness of block A and B (hence a zero-path-length difference between the vertical and horizontal polarization), the relative optical delay between the two replicas is given by:

$$\tau = \frac{\Delta n(\nu) x \sin \alpha}{c}. \tag{1}$$

It is important to note that this delay is independent of the beam size. This will be of crucial importance when dealing with image formation. However, this is not true for a beam that travels inside the interferometer with a different propagation angle.

Since the birefringence of the crystal is frequency-dependent also the delay depends on it. This marks a difference with respect to double-beam interferometers made of mirrors (Michelson and Mach–Zehnder). We will discuss the consequences in the next section.

Block B's gap should be typically minimized to avoid chromatic dispersion and loss of interference modulation down to approximately 1 mm. However, the gap shown in figure 1 does not introduce any appreciable channel fringing due to interference between the main and the forward reflected beam. This is because the optical delay between the two beams is way more than the maximum optical delay introduced by this CPI. Moreover, these beams are shifted by a non-negligible amount considering the typical coherence diameter of spatially incoherent sources such as the one employed in the applications described in this manuscript and they cannot appreciably interfere. In general, these reflections can be minimized by using an anti-reflection coating or by tuning the alignment of the CPI, especially of block B's wedges.

2.2. Differences with respect to a Michelson's interferometer

In a Michelson's interferometer, the electromagnetic radiation is split into two beams by a beam-splitter. The two replicas travel along distinct paths (arms), and after bouncing back into two mirrors, they recombine into one beam interfering at the sample or detector. By moving one of the two mirrors, we can change the relative path-length difference, introducing an optical delay between the two radiations. The following equation gives the interference signal as a function of the delay as measured by a detector, and it defines the so-called interferogram:

$$I(\tau) = \Big\langle \int \big| \tilde{E}(\nu, t) + \tilde{E}(\nu, t) e^{-i2\pi\tau\nu} \big|^2 \, d\nu \Big\rangle, \tag{2}$$

where $\tilde{E}(\nu)$ is the electric field of electromagnetic radiation as a function of the frequency ν, the rhs addendum is the delayed replica of the radiation, the integration along ν is performed to take into account the spectral blindness of the detector, and the angle brackets are used to indicate an average over time. This interferogram represents an auto-correlation signal, and for the Wiener–Khintchine theorem [12, 13] by doing a Fourier

transformation, we obtain the spectrum:

$$\tilde{S}(\nu) = \int I(\tau)\, e^{i2\pi\nu\tau}\, d\tau.$$

Considering the previously described CPI, the formalism is slightly different because, as highlighted in the equation (1), the delay is frequency-dependent. To account for this dependence, the equation (2) as to be changed into:

$$I(x) = \left\langle \int \left| \tilde{E}(\nu, t) + \tilde{E}(\nu, t)e^{-i2\pi\tau(\nu, x)\nu} \right|^2 d\nu \right\rangle =$$
$$\left\langle \int \left| \tilde{E}(\nu, t) + \tilde{E}(\nu, t)e^{-i2\pi\frac{\Delta n(\nu)\sin \alpha x}{c}\nu} \right|^2 d\nu \right\rangle, \tag{3}$$

where we introduce the explicit dependence of the delay from the frequency ν and the wedge position x. As a result, the interference signal is now dependent on x.

If a one by one relationship between the birefringence Δn and the frequency ν is granted, the Wiener–Khintchine theorem [12, 13] still holds, and we can compute the spectrum as:

$$\tilde{S}(f_x) = \int I(x)e^{i2\pi f_x x}\, dx, \tag{4}$$

where f_x is the spatial frequency. This variable is the Fourier pair-variable of x, and it shares the same dependencies on the parameters of the CPI, namely on Δn and on α. Therefore, we need to convert the spectrum $\tilde{S}(f_x)$ into the corresponding $\tilde{S}(\nu)$. This can be done by an abscissa conversion from the spatial frequency f_x to the optical frequency ν (a spectral calibration of the device) and a Jacobian conversion to ensure energy conservation.

It is important to note that the level of accuracy and stability reached by this common-path device is very high compared to a common Michelson's interferometer due to the uncorrelated mechanical vibrations of the two mirrors and the difficulty in maintaining the required alignment of the moving mirror within a range of few μrad. Indeed, in the CPI, the two replicas travel along the same path and experience the same perturbations from the environment. Therefore, the absolute arrival path of the two changes but not the relative path difference, which is the crucial factor in FT spectroscopy. The relative delay accuracy of the CPI is demonstrated [8] to be in the order of few attoseconds.

The stability of the interferometer is exceptionally high. This is due to a de multiplying factor that decreases the effective path length change in response to a moving wedge movement along the x axis. Indeed, in a Michelson's interferometer, moving one mirror by an x amount increases the path length difference by two times this quantity ($2x$). In the CPI, moving the wedge by an x amount introduces a path length difference of $\Delta n \sin \alpha x$. The ratio between the two path length differences is $2/\Delta n \sin \alpha$, which is typically in the order of 100–120. Therefore, a positioning error introduces an uncertainty in the interferometric delay, which is two orders of magnitude less than the one of a Michelson's interferometer.
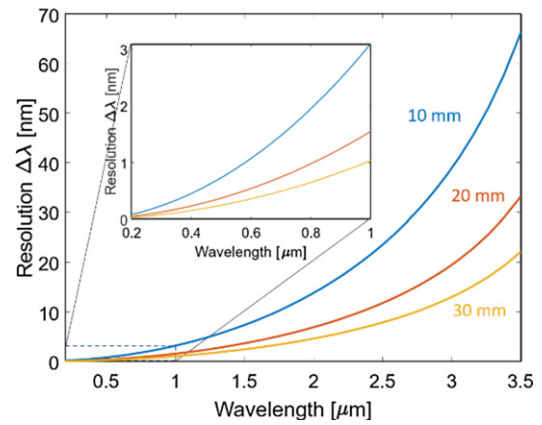

Figure 3. Three curves are plotted for different scan lengths (10, 20 and 30 mm) of the interferometer. Birefringent material: alpha-BBO (α-barium borate, BaB_2O_4).

2.3. Spectral resolution

In an interferometer, the maximum scan position of the device determines the spectral resolution. The longer the distance between this position and the zero delay, the better the spectral resolution. The spectral resolution is related to the maximum excursion by [14]:

$$\Delta\nu = 0.605\frac{1}{\tau_{max}}, \tag{5}$$

where $\Delta\nu$ is the spectral resolution and τ_{max} is the maximum delay of the interferometer. Alternatively, in the wavelength domain:

$$\Delta\lambda = 0.605\frac{\lambda^2}{\tau_{max}c} = 0.605\frac{\lambda^2}{\Delta n x_{max} \sin \alpha}, \tag{6}$$

where $\Delta\lambda$ is the spectral resolution expressed in the wavelength domain. The spectral resolution has a similar λ^2 dependency on the light wavelength as Michelson's interferometer, but another smaller spectrally dependent contribution comes from the birefringence of the used crystalline material.

As an example, figure 3 displays the variation of the spectral resolution across the transmission range of the birefringent crystal. It shows three different curves for a 10 mm, 20 mm, and 30 mm interferometer excursion range. Since the operating range of the interferometer is remarkably big, the spectral resolution changes considerably.

2.4. Spectral calibration

The CPI's spectral calibration is a procedure that converts the spatial frequency axis f_x to the optical frequency one ν. Mathematically, the aim is to find a relationship F so that $v = F(f_x)$. To retrieve this transformation, we can consider a monochromatic light beam of frequency $\overline{\nu}$. By moving one of the two birefringent wedges and recording the interference signal's intensity as a function of the position x, we can measure the interferogram $I(x)$.
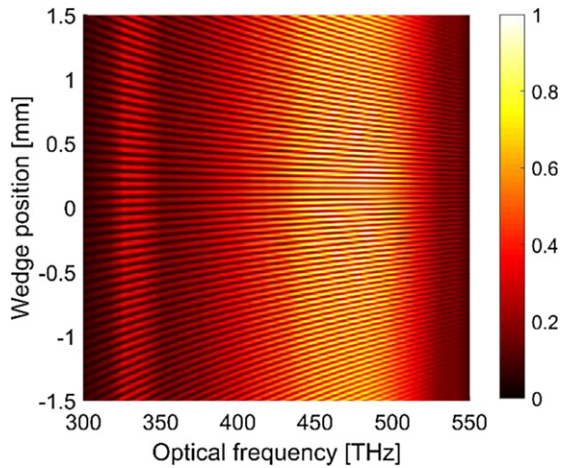
Figure 4. This map was measured with a dispersive spectrometer placed at the exit of the interferometer, and it shows the output spectrum as a function of the wedge position. Each column of this map corresponds to an interferogram at a specific optical frequency.

Figure 5. This intensity map shows the result of a column-by-column Fourier transformation of the measured map of figure 4. The circles underline the curve, derived using the formula (8). This intensity map is used as a look-up table to convert from spatial to optical frequencies.

Since we are dealing with a monochromatic beam, according to the equation (1), the recorded signal will be a perfect sinusoidal wave with a spatial period X between each consecutive peak of the sinusoidal function given by:

$$X = \frac{c}{\Delta n(\overline{\nu}) \times \sin \alpha \times \overline{\nu}}. \tag{7}$$

By doing a Fourier transformation of this signal, we retrieve a spectrum that peaks at a correspondent spatial frequency $\overline{f_x}$, found to be:

$$\overline{f_x} = \frac{\Delta n(\overline{\nu}) \times \sin \alpha \times \overline{\nu}}{c}. \tag{8}$$

This equation is valid for each pair $\{\overline{f_x}, \overline{\nu}\}$ and can be measured experimentally by employing a broadband light source and measuring for each position of the moving wedge the light spectrum after the propagation inside the interferometer.

By stacking together the spectra row by row, we can build a map such as the one in figure 4, where each column represents the sinusoidal interferogram of the corresponding optical frequency read in the abscissa axis. By performing a Fourier transformation column by column, we can retrieve the intensity map in figure 5. The map's intensity peaks forming a curve, which is indeed a visual representation of the measured relationship shown in equation (8). The white circles underline the theoretical curve obtained from the equation (8) by inserting the measured α value and the employed material's birefringence from its tabulated Sellmeier equations. As expected, the overlap between the two is excellent.

Inverting the equation (8), we found mathematically the relationship F we were looking for as:

$$\nu = F(f_x) = \frac{c \times f_x}{\Delta n(f_x) \times \sin \alpha}. \tag{9}$$

From it, we can convert from the spatial frequency axis f_x, which is the natural axis of the CPI, to the optical frequency axis.

This conversion is experimentally done using the map in figure 5 as a look-up table between the two-frequency axis.
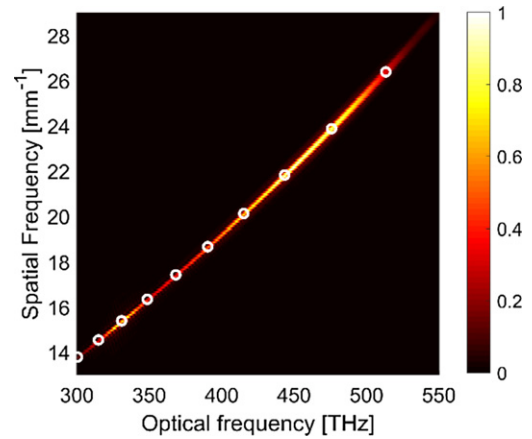
This procedure can be done by a polynomial interpolation where the aim is to find a set of polynomial coefficients $\{P_i\}$ such as $\nu = F(f_x) = \sum_1^n P_i f_x^i$. Or by a more complex piecewise linear interpolation. This calibration procedure is only dependent on the chosen birefringent crystal and its geometrical shape, namely the wedge apex angle value. In the absence of a spectrometer, especially in the infrared spectral ranges where they are expensive, it is possible to use the same spectral calibration procedure utilizing a set of interferential filters by measuring several known laser lines or by using a spectrally calibrated sample.

2.5. Intensity calibration

After the spectral calibration procedure explained in the last section, it is also essential to perform an intensity calibration procedure. Indeed, to ensure energy conservation, we need to impose that $\tilde{S}(f_x)\mathrm{d}f_x = \tilde{S}(\nu)\mathrm{d}\nu$ or equally [15]:

$$\tilde{S}(\nu) = \tilde{S}(f_x)\frac{\mathrm{d}f_x}{\mathrm{d}\nu}. \tag{10}$$

To evaluate the differential form in the last equation, we need to consider the equation (8) again, thus obtaining:

$$\mathrm{d}f_x = \frac{\mathrm{d}\Delta n(\nu)}{\mathrm{d}\nu}\frac{\nu \sin \alpha}{c}\mathrm{d}\nu + \frac{\Delta n(\nu)\sin \alpha}{c}\mathrm{d}\nu, \tag{11}$$

by inserting this result into the equation (10), we arrive at the following relationship:

$$\tilde{S}(\nu) = \tilde{S}(f_x)\left(\frac{\mathrm{d}\Delta n(\nu)}{\mathrm{d}\nu}\frac{\nu \sin \alpha}{c} + \frac{\Delta n(\nu)\sin \alpha}{c}\right). \tag{12}$$

It is important to note that this intensity calibration does not play a role when the physical entities to be measured are expressed as ratios (transmittance, absorbance, reflectance, etc) since the numerator and denominator corrections cancel each other. Since the correction is strongly wavelength-dependent, the effect is especially evident when the light's

spectral range is broad (e.g., thermal radiation), while it is negligible when a narrowband source is measured (e.g., a laser). The birefringence as a function of the optical frequency $\Delta n(\nu)$ that appears in the expression (12) can be experimentally measured by acquiring the calibration map of figure 5. Then it is numerically extracted by inverting the relationship (9).

2.6. Interferometric calibration

In the interferometric approach, the detector measures the interference signal as a function of the position. Then, an FT retrieves the spectrum. Considering the CPI, an optical encoder, built-in the linear stage, measures the moving wedge's position. The result has high accuracy at the linear stage level, but the values might differ from the moving wedge's real position. This is generally due to imperfections of the wedge mounting, reproducible errors in the encoder readings, and of the linear stage. To solve this issue, we can measure the interferometer's correct position values from a narrowband laser source's interference signal. Notably, due to the high reproducibility and accuracy of the CPI, we need to perform this procedure once. Then, its result works for all the following measurements. Indeed, a pure sinusoidal function describes the interferogram of a monochromatic light source entering the interferometer:

$$y_n = \cos(a \cdot x_n), \qquad (13)$$

where the subscript n indicates the sampling steps. a is the angular frequency corresponding to the optical frequency of the monochromatic wave and x_n is the correct position. The interferogram measured with the CPI as a function of the position as read by the optical encoder slightly deviates from a pure sinusoidal function. This is because the position reads are not accurate enough. However, from the measured interferogram, we can retrieve the correct interferometric position axis. Indeed, the equation (13) can be recast as:

$$y_n = \frac{1}{2}\left(e^{iax_n} + e^{-iax_n}\right). \qquad (14)$$

In the spectral domain, this equation becomes:

$$y(f) = \frac{1}{2}\left[e^{i2\pi(f+a)} + e^{i2\pi(f-a)}\right] \qquad (15)$$

filtering out the negative frequency term and performing an inverse FT, it is possible to isolate the first complex exponential of the equation (15): by isolating only one of the two exponential terms, we can easily retrieve the correct position from the phase of $\bar{y}_n$.

To show this method's capability, we used a He–Ne laser as a monochromatic light source, and we retrieved the calibrated position array x_n. Figure 6(A) shows the result, where the position deviation between the calibrated and the measured one is plotted with respect to the interferometer position.

The position error is around 4×10^{-2} μm over the whole scan range of the interferometer. Figure 6(B) shows how this calibration impacts the spectral accuracy of the measurement. The He–Ne laser spectrum is computed using the calibrated axis, or the position axis read from the motor
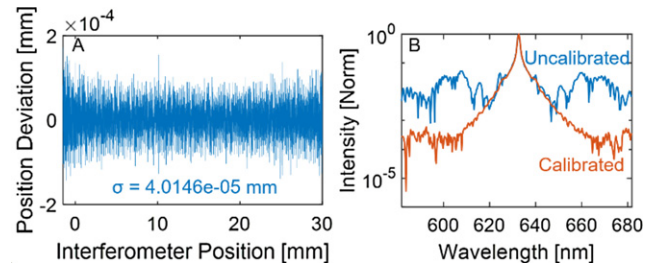

Figure 6. (A) This figure shows the position deviation as retrieved with the interferometric calibration algorithm with respect to the interferometer position as read by the encoder. (B) Spectrum of He–Ne laser source computed using the calibrated axis, or the position axis read from the motor encoder.

encoder. Notably, the reduction in the background level is as high as 200 times. Remarkably, the position deviation pattern remains stable across multiple scans. This clearly shows that the positioning error is highly reproducible. Therefore, once the position deviation is measured, it is possible to correct the encoder position values without keeping an inline reference laser.

3. Fluorescence spectroscopy

In fluorescence, a molecule absorbs light from a source, and then after some typical time called fluorescent lifetime, it emits light at longer wavelengths. This phenomenon carries information in the excitation, emission, and temporal behavior. Therefore, it can be used to identify and observe quantitatively the different chemical species comprising the sample. It is widely used in academia and industry thanks to its high sensitivity, simplicity, and specificity.

Figure 7 represents the typical scheme describing the fluorescence emission process. This kind of scheme is typically called Jabłoński diagram in honor of the pioneering works of the Polish physicist Aleksander Jabłoński in the molecular spectroscopy and photophysics fields [16]. As depicted in the scheme, the first step of the process is the absorption of a photon from the incoming radiation. As a result, the fluorescent molecule is excited and leaves its ground electronic state in favor of one of the various vibrational levels in the excited electronic state. After the excitation, collisions and interaction with other molecules comprising the sample cause the excited molecule to exchange its energy with the environment with the effect of losing its vibrational energy, and the molecule rapidly drops down to reach the lowest vibrational state of the excited electronic state. After some time, the fluorescence emission of a photon occurs from this vibrational state, and the molecule gives in this way part of its energy to the fluorescence electromagnetic field. As a result, the molecule reaches one of the various vibrational levels of the ground electronic state. This process is intrinsically stochastic, and the molecules may drop down into any of several vibrational levels in the ground state with a different probability described by the laws of quantum mechanics. Consequently, for the energy conservation law to hold, the emitted photons will have different energies, hence
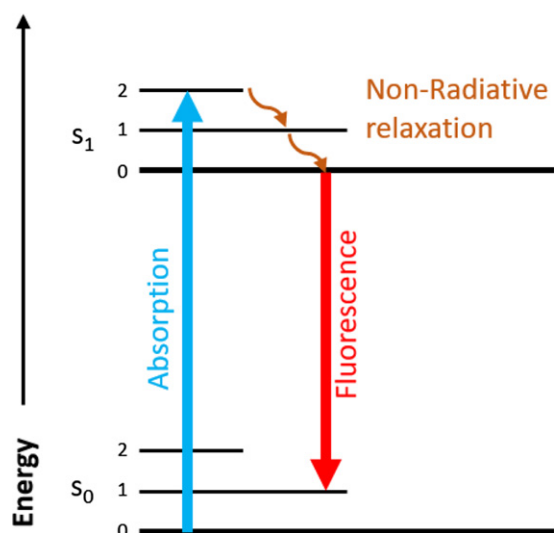
Figure 7. Energy scheme of the fluorescence emission, the so-called Jabłoński diagram.

Figure 8. (A) Emission fluorescence spectroscopy setup (top). Energy scheme of the involved transitions (bottom). (B) Excitation fluorescence spectroscopy setup (top). Energy scheme with the involved transition (bottom).

frequencies. Therefore, as an example, it is possible employing a spectrometer to analyze the intensity of the fluorescence emission at different frequencies and access to the structure of the different vibrational levels of the molecule.

3.1. Measurement of excitation–emission-matrix (EEM) maps

Fluorescence spectroscopy is a powerful technique for the physical and chemical analysis of solids, liquids, and nanostructures [17]. It has a high sensitivity down to the single-molecule limit [18] and a broad range of applications. It has been used in biology and medicine [19], for food quality assessment [20], for environmental analysis [21], for crime scene investigation [22], and to monitor artworks conservation [23]. There are mainly two techniques to analyze the sample fluorescence spectrally. In emission fluorescence spectroscopy, the excitation wavelength is kept fixed, and the detection wavelength varies.

Figure 8 shows that this technique detects the emission from the lowest vibrational state of the excited electronic state to the vibrational levels of the ground electronic state and gives information on the latter. We can extract structural information about the molecules in their excited state. Differently, in a fluorescence excitation measurement, the detection wavelength is fixed, and the excitation wavelength is varied across a region of interest. This technique gives information on the vibrational levels of the excited electronic state. Since with this technique we extract information about the excitation behavior of the fluorescent molecules, and the excitation happens when the molecules are in their ground state with this technique, it is possible to extract information on the molecular structure of the emitters when they are in the ground state, the most probable one. Both techniques are useful tools to analyze samples, and it is possible to combine the two into a single one by measuring the emission spectrum of the sample at each excitation wavelength and combining them all into a so-called EEM map. These EEM maps are handy tools, and,
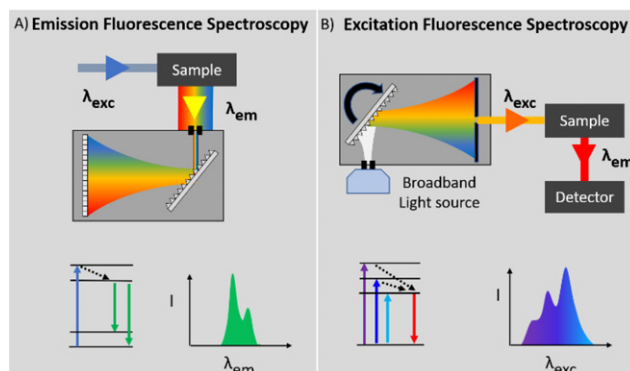
as an example, they are used to study energy transfers between fluorescent molecules [24]. Since EEM maps provide information on the excitation and emission behavior of the sample, we can use them to disentangle the contribution of different chemical species to the emission of the sample both in gas [25, 26] and condensed phase [20, 21, 27–30]. This information is beneficial in quality control or food and environmental analysis [20, 21, 27]. However, the excitation wavelength scan requires bulky monochromators, and only a small portion of the light reaches and excites the sample. This leads to long integration times. For this reason, a broadband interferometric technique has been recently developed [31–33]. This solution combines the many advantages of Fourier-transform spectroscopy to the ability to excite the sample with all the wavelengths simultaneously, resulting in low integration times and accurate excitation spectra. The interferometric approach has been used by Hirschberg *et al* using a double beam interferometer and a photomultiplier tube to detect the sample fluorescence [31]. Peng and collaborators used this approach to measure the fluorescence excitation spectra and the dependence of the fluorescence lifetime to the excitation wavelength [34]. Piatkowski and colleagues used the interferometric method to investigate single molecules' peculiar excitation spectra compared to the ensemble emission [33]. Anzai *et al* pioneered using the interferometric approach to record the EEM maps of fluorescent samples [32]. The interferometric measurement of these maps is challenging because it requires measuring an emission spectrum for each interferometer delay. The delay must be stabilized and kept fixed for all the integration time needed to measure the emission. This means that the interferometer's path-length difference must not fluctuate during the measurement of more than a few tenths of the excitation wavelength. This is especially hard using visible and ultraviolet excitation light sources. This is the main reason that prevented using an ordinary double-beam interferometer such as a Michelson's one to measure EEM maps. Anzai *et al* brilliantly circumvented this issue by using a tandem Fabry–Perot interferometer.

In this setup, one Fabry–Perot interferometer is kept fixed, while the other one varies its cavity length. This generates a

J. Phys. B: At. Mol. Opt. Phys. **54** (2021) 113001

A Perri

variable beating in the incoming light, effectively modulating the excitation light. This approach is compact and straightforward, but it has many drawbacks. The presence of high-frequency spectral fringes spoils the signal. These fringes are intrinsic in the method and result from the spectral interference inside the Fabry–Perot cavity. The variation of the tunable Fabry–Perot interferometer's cavity length is limited to a few tens of microns. This affects the system's spectral resolution, limiting its use in the analysis of congested fluorescence spectra. The motor that moves the mirror in the Fabry–Perot cavity must have a nano-metric resolution and accuracy, increasing the system's cost and complexity. The use of two Fabry–Perot interferometers comprising of four transmitting mirrors decreases the light throughput of the system. This is critical because the light throughput is crucial and determines the final sensitivity of the instrument. Since the known technique shows limitations in resolution, stability, and light throughput, we developed a new setup comprising the previously described common-path birefringent interferometer.

3.1.1. Measurement principle. In the interferometric technique, the excitation light coming from a broadband source passes through an interferometer. The interferometer generates two interfering replicas of the incoming light separated by a controllable delay. After the interferometer, the light pair interferes, and as a result, the output light spectrum is variably modulated depending on the delay imposed by the interferometer. This is especially evident by analyzing the interference signal of two identical fields in the frequency domain. We already introduced it as the argument of the equation (2), reported here for convenience:

$$\left| \tilde{E}(\nu) + \tilde{E}(\nu) e^{-i2\pi\tau\nu} \right|^2 \tag{16}$$

by computing the magnitude squared, we obtain:

$$2\left| \tilde{E}(\nu) \right|^2 + 2\Re \left\{ \left| \tilde{E}(\nu) \right|^2 e^{-i2\pi\tau\nu} \right\}. \tag{17}$$

Furthermore, by computing the real part, we obtain:

$$2\left| \tilde{E}(\nu) \right|^2 + 2\left| \tilde{E}(\nu) \right|^2 \cos(2\pi\tau\nu). \tag{18}$$

The output light spectrum is therefore modulated in the spectral domain with a variable period $1/\tau$. Figure 4 shows a map obtained by stacking together many spectra (recorded by a spectrometer), each at a different delay (position of the interferometer). As we can see by looking at the map column-wise, each frequency has a different modulation period in the interferometer position axis. By performing an FT column by column, we can calculate this modulating period for each wavelength, as shown in figure 5. If we consider a fluorescent sample absorbing at a specific wavelength, its fluorescence emission will be linearly dependent on the electromagnetic field's intensity at that excitation wavelength. Therefore, if we use the light at the interferometer's output to excite the fluorescent sample since the excitation intensity is periodically dependent on the interferometer's delay, the sample emission intensity will be identically dependent on the delay. Thus, it
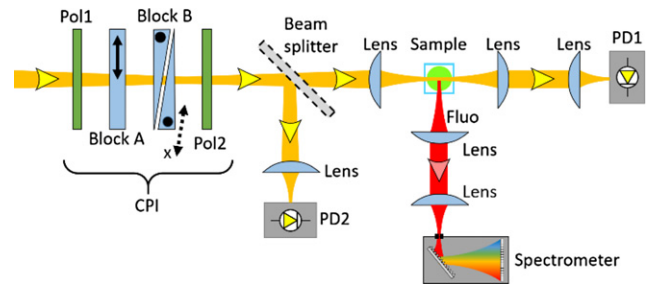

Figure 9. This figure shows a basic scheme of the developed EEM/absorption spectrometer. Reproduced with permission from [35]. © 2017 Optical Society of America.

is possible by recording the emission intensity of the sample as a function of the delay to retrieve the information on the excitation behavior of the sample. We can accomplish this by performing an FT of the fluorescence emission intensity as a delay function. Hence, the result highlights the contribution of each excitation wavelength to the fluorescent emission.

3.1.2. Experimental setup. Figure 9 shows the experimental setup of the developed EEM/absorption spectrometer [35]. The light from a broadband source passes through the interferometer and excites a fluorescent sample. The emission light is collected at 90° to reject the excitation light collection that otherwise overwhelms the weak fluorescent emission. Finally, the collected light is focused on a grating-based spectrometer. Thanks to the interferometer's common-path nature, it was possible to excite the samples with both a coherent and an incoherent light source [35]. A 50% beam splitter located at the exit aperture of the interferometer splits the intensity into two paths. The reflected beam is focused on a photodiode (PD2), measuring the reference interferogram $I_{ref}(\tau)$, while the transmitted one is focused on the sample contained in a 1 cm thick quartz cuvette. The light transmitted by the sample is focused on another photodetector (PD1, identical to PD2), measuring the transmission interferogram $I_{trans}(\tau)$. The fluorescence emission, collected at 90°, collimated and focused on a grating-based spectrometer measuring the delay-dependent fluorescence spectrum $I_{fluor}(\tau, f_2)$, where f_2 is the emission frequency. By computing an FT of the delay-dependent fluorescence spectrums with respect to τ, one obtains the two-dimensional EEM map $\tilde{I}_{fluor}(f_1, f_2)$. A reference measurement with a pure solvent in the cuvette holder is often required to retrieve $A(f_1)$, as described by [36]. This is due to differences in the two detector's responsivities, PD1 and PD2, and further losses (mainly Fresnel reflections) along the two optical paths. This allows us to compute a frequency-dependent calibration curve $c(\omega_1)$ so that the absorption spectrum is:

$$A(f_1) = -\log \left(\frac{c(f_1)\tilde{I}_{trans}(f_1)}{\tilde{I}_{ref}(f_1)} \right). \tag{19}$$

Where $\tilde{I}_{trans}(f_1)$ and $\tilde{I}_{ref}(f_1)$ are the result of a Fourier transformation of the signal $\tilde{I}_{trans}(\tau)$ and $\tilde{I}_{ref}(\tau)$, respectively.

The reference path's presence is also useful to some extent to reject the noise coming from the light source intensity fluctuations.
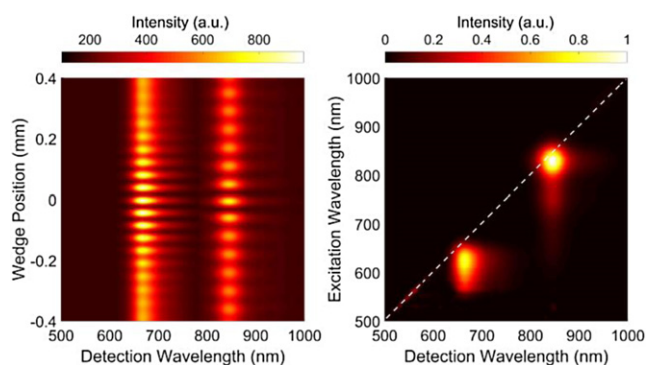
J. Phys. B: At. Mol. Opt. Phys. **54** (2021) 113001

A Perri

Figure 10. (a) Zoom of the interferometric map of the mixture of the dyes Nile Blue and IR820 as a function of emission wavelength and interferometer position x. The complete map is composed of 800 emission spectra acquired at a different delay. The delays were equally distributed in a 4 mm interferometer excursion range. The integration time for each emission spectrum was 1 s. The full map was acquired in 800 s (b) 2D EEM map as a function of excitation and emission wavelengths, obtained by performing the FT of the map in (a) with respect to x. This map is calibrated both in intensity and spectrally. The employed light source was a supercontinuum fiber laser (NKT Photonics model SuperK Extreme EXW-12).

3.1.3. Results. EEM maps show their potential when applied to a mixture of fluorescent chemical species. These kinds of maps can be used to disentangle the contributions of each emitter. This is true also when the absorption or the emission of several species overlaps. For this reason, we measured a mixture of two dyes, Nile Blue and IR820 dissolved in methanol. The absorption spectrum of the used mixture was measured by a commercial spectrometer showing a maximum optical density for the two dyes of 0.1 and 0.45, respectively. These optical densities were chosen to compensate for the different fluorescence quantum yields of the two dyes, thus matching the emission intensities.

Figure 10 shows the measurement result. The map in the left part of figure 10 is the interferometric map composed by stacking together several emission spectra at a different delay of the interferometer. It is evident how two interference patterns dominate the map. The first one is located around $\lambda_2 = 650$ nm in the emission wavelength axis, and it belongs to the Nile Blue contribution. The other at $\lambda_2 = 850$ nm is related to the IR820. The two patterns have different periodicities along the interferometer's position axis, highlighting their different excitation behaviors.

Indeed, the map in the right part of figure 10 shows the resulting EEM after a column by column FT has been performed. Each column has been normalized for the excitation source spectrum. Despite the two dyes absorptions being partially overlapped, the map disentangles the two chemical species' contributions. As expected, the two intensity peaks are located at longer wavelengths with respect to their excitations, so the two dyes' contributions are located below the map diagonal. A small portion of the IR820 intensity peak is exceeding the diagonal line. This is an artifact due to the limited excursion range employed. We could not demonstrate any energy transfer process in the solution. This is because the two dyes' concentration inside the solution was too low to guarantee a distance

between the donor–acceptor pair, which was sufficiently small for the effect to be visible. Moreover, it is essential to note that the spectral overlap between the donor emission and the acceptor absorption is low, lowering the energy transfer process's yield.

The system has clear advantages with respect to existing wavelength scanning technologies being faster, more compact, and more straightforward. This is determined by the large entrance aperture of the CPI and the use of all the source light spectrum to excite the sample and not only a small portion of it.

3.2. Single-molecule EEM

Single-molecule spectroscopy (SMS) techniques are unique tools able to reveal quantitative properties of single emitters and local nanoscopic environments. This degree of information is usually lost when bulk samples are measured. Substantial technological improvements have changed a lot the SMS field in the last two decades. However, measuring excitation spectra of individual molecules, especially at lab temperature, still poses a significant challenge. To solve this problem, we applied the CPI to a single molecule spectroscopy setup. We use a CPI and broadband excitation to simultaneously measure the fluorescence emission and excitation spectra. We used the technique to measure room-temperature excitation and emission spectra of individual terrylene diimide molecules.

3.2.1. Experimental setup. Figure 11 shows a schematic of the experimental setup. A broadband supercontinuum source excites the sample. The excitation light passes through a CPI (GEMINI, NIREOS s.r.l.) that modulates its spectrum. A short pass optical filter filters the light before entering the confocal microscope. The objective focuses the light on the sample, and it collects the emission. A long-pass filter rejects the excitation light and selects only the weak fluorescence emission. Finally, a flip mirror reflects the emission toward a nitrogen-cooled spectrograph or a time-correlated single photon counting system (TCSPC). This last branch of the setup is composed of two avalanche photodiodes and a 50:50 beam-splitter. It was used to measure time-resolved excitation map, acquire spatial maps of the sample, localize the emitters, and perform photon anti-bunching tests to demonstrate single-molecule emission.

3.2.2. Results. To demonstrate the experimental setup's capability, we measured EEM and time-resolved excitation maps of terrylene diimide. We selected this sample because of its high stability at room temperature and good quantum efficiency. The details on sample preparation and experimental setup can be found in reference [37]. Figure 12 shows the experimental results. We measured a single-molecule fluorescence emission spectrum at each step of the interferometer. Panel (a) of figure 12 shows the interferometric map obtained by stacking together all these spectra. By performing a Fourier transformation row by row, it is possible to retrieve the excitation–emission map shown in figure 12(B). It is important to note that it was impossible to measure the full emission and excitation axis simultaneously. This is because of the small Stokes shift of the terrylene diimide molecules. Indeed,
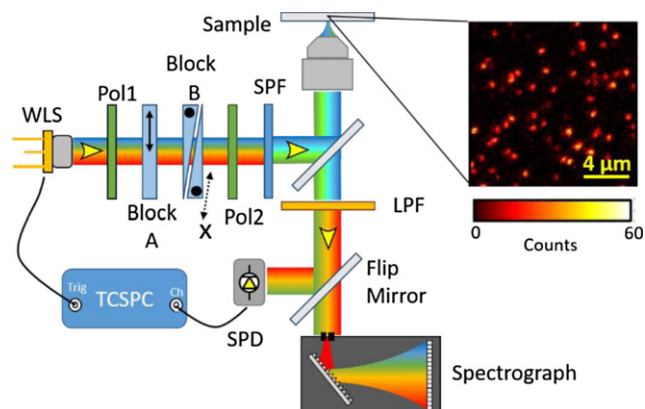
Figure 11. Experimental setup used to measure EEM maps of single molecules at room temperature. The top right part shows an image of the sample obtained by raster scanning while measuring the avalanche detector signal. Each bright spot highlights a single molecule.
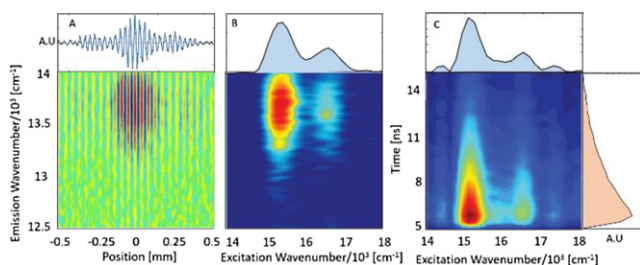

Figure 12. (A) Interferometric map built by stacking together all the emission spectra correspondent to each specific interferometer position. (B) EEM map of a single terrylene diimide molecule at room temperature. The map was cut in the emission axis at $14\,000$ cm^{-1} by using a filter because of the small Stokes shift of the molecule. (C) Time-resolved excitation map of the same single molecule.

Figure 13. Panel (A) visualizes several emission (red) and excitation (green) spectra of terrylene diimide molecules. These spectra were directly extracted from the EEM matrices. (B) A statistical representation of the distribution of transition frequencies. (C) This figure shows a representation of the distributions of 0–0 transition linewidths for the emission (red) and excitation spectra (blue). (D) Distribution of Stokes shifts among the different measured molecules.

figure 12(B) shows the full excitation axis, while the emission ends at 14 000 cm^{-1}. Panel (c) of figure 12 displays the time-resolved excitation map of the single molecule. The TCSPC system measures a complete time-decay curve for each delay of the interferometer. A simple FT of the map along the interferometer's position axis produces the map of the panel (c).

Figure 13 displays a representative selection of excitation and emission spectra for different chemically identical single molecules. As it is possible to see, every single molecule has peculiar spectral features in both the excitation and emission axis. Namely, it is possible to extract meaningful statistical information about the distribution of the transition levels, the linewidths of spectral peaks, and the Stokes shifts. This high variability is usually missed when looking at the ensemble level. It gives precious information about single-molecule interactions with the nanoscopic local environment. It is important to note that the presented technique applied to SMS can be less sensitive than the wavelength scanning ones to single molecules' blinking. Indeed, if blinking occurs while performing an excitation wavelength scan, the resulting
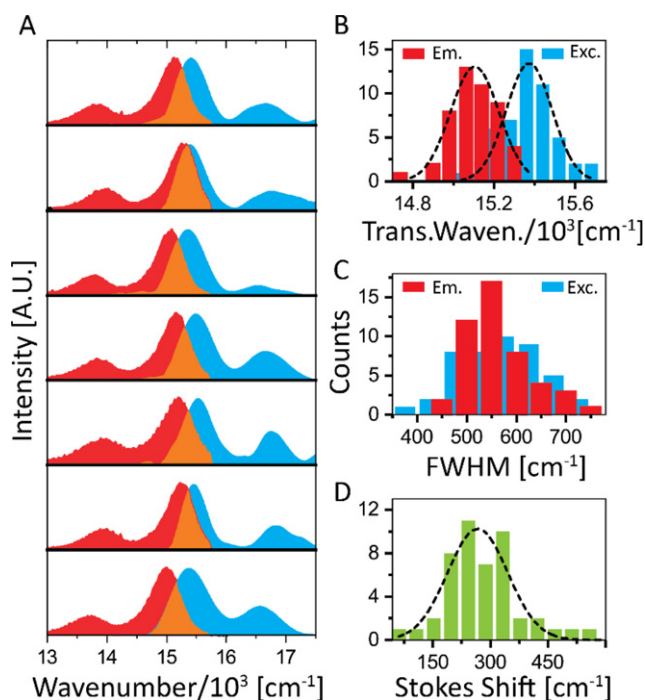
spectrum is spoiled by low values at the wavelengths corresponding to the scan time the blink has occurred. If the same happens during the scan of the CPI, since the spectral information is retrieved from all the steps' contribution, the perturbation introduces only some noise. This noise is evenly spread across the spectrum.

3.3. Time-resolved fluorescence spectroscopy

The spectral study of fluorescence is a powerful and widely used technique. This is due to its simplicity and the very high sensitivity of commercially available detectors, in some cases, capable of detecting single photons. However, fluorescence carries information not only in the spectral domain but also in the temporal one. Sometimes, the study of fluorescence time dynamics can retrieve information about the sample that is not available from spectroscopic data alone. This is especially true for congested samples or when it is crucial to discriminate the emitters of interest from other chemical species' backgrounds or emissions. However, the temporal behavior to be recorded is typically very fast, posing significant technological challenges. The typical fluorescence decay duration of organic emitters is from a few hundred picoseconds to a few hundred nanoseconds. For this reason, it is tough for existing electronic devices to record this decay from a single excitation event. This is because a reasonable amount of samples are needed to resolve the typical exponential fluorescence decay. For this reason, the sampling rate of the acquisition system must be in the order of

J. Phys. B: At. Mol. Opt. Phys. **54** (2021) 113001

A Perri

some tens of giga-samples per second. Moreover, we need to consider that the fluorescence signal might be so low to consist only of single photons per excitation event. In this case, the discreteness of the signal itself prevents the analog sampling of the decay. This is the typical case of SMS.

Many techniques have been developed to acquire the fluorescence signal as a function of time. They have different levels of temporal resolution. The fastest methods use an ultrashort laser pulse to perform fluorescence gating [38, 39] or upconversion [40–42], enabling a resolution of hundreds of femtoseconds. However, the experimental complexity of these methods is very high, and the sensitivity is reduced. When the temporal requirements are not so high, it is possible to use streak cameras [43, 44]. These devices permit a high temporal resolution around a few picoseconds, but they are costly and fragile instruments. Another solution to measure this fast decay is similar to the one used by English-American photographer Edward James Muggeridge to make sense of the galloping horse's motion in 1878. The idea is to use periodic excitation from a fast, impulsive light source and to collect for each excitation cycle the relative time from excitation to the detection of a single emission event. By recording these start-stop times for many cycles, thus for many different events, it is possible to reconstruct the sample temporal behavior. This is performed with the same result as possible using an ideally fast enough electronic acquisition system, used to follow the decay of a single excitation event. This technique is called TCSPC [45, 46] and permits a temporal resolution down to a few tens of pico-seconds. It is based on the accurate cyclic timed acquisition of single photons from the fluorescence emission with respect to the excitation pulse. Figure 14 presents the operating principle, an impulsive excitation with a specific repetition-rate, excites the sample. The time between each excitation pulse and the detection of a photon emitted after the fluorescence de-excitation is recorded. A histogram visualizes these times revealing the temporal fluorescence decay of the sample.

Unfortunately, single-photon detectors and electronics have a so-called dead time in which, typically for some tens of nanoseconds, they cannot detect other photons. For this reason, TCSPC systems permit only one photon count per single excitation cycle. This prevents uneven registration leading to the over-representation of early fluorescence photons. However, since it is possible to count only one event per cycle, it is important to keep low the probability of detecting more than one photon per excitation [47]. This is because if more than one photon is generated per cycle, only the first one will be correctly counted. This introduces artifacts in the measured temporal histogram. The early photons have more probability of being registered, and they are over-represented in the measured fluorescence decay, thus invalidating the result. For this reason, the excitation power is reduced to a level in which the probability for the detector to measure more than one photon per cycle is low. Typically, the fluorescence photon count rate must be at most 1% of the excitation's repetition rate. Thus, only one in a hundred excitation pulses should generate a fluorescence
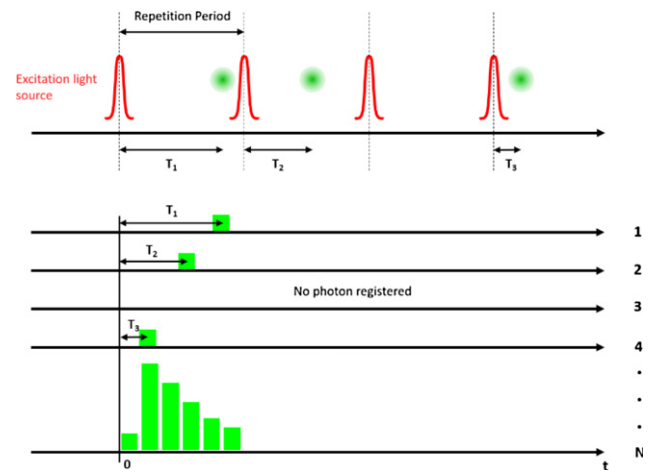

Figure 14. Basic principle of the TCSPC method. The time between each excitation pulse and the detection of a photon emitted after the fluorescence de-excitation of the sample is recorded repetitively. After N excitation/emission cycles, all the start–stop times are stacked and represented in a histogram. This histogram reveals the temporal fluorescence decay of the sample.

photon detection event. To have a good signal-to-noise, a histogram typically contains millions of events, the typical acquisition time of a single time trace is in the order of seconds. It is important to note that typically, the excitation light source's repetition rate determines the maximum possible duration of the time decay to be measured. This is because the TCSPC electronics detect only the relative time between an excitation laser pulse and a photon's measurement by the single-photon detector. The time difference cannot exceed the light source repetition period. Indeed, after a new excitation light pulse is detected, the TCSPC start–stop time starts again from zero. Therefore, the detected photon is incorrectly assigned to belong to the lastly detected excitation pulse.

3.3.1. Measurement time-resolved photoluminescence (TRPL). For complex samples, the temporal information alone is not sufficient to study the whole fluorescence behavior. It is possible to combine the temporal and spectral information by placing a monochromator in front of the detector and collecting a series of histograms corresponding to different emission wavelengths. Then, these histograms can be grouped into a map creating a so-called time-resolved emission spectra (TRES). It is also possible to proceed in parallel, increasing the setup's complexity and cost, using a single TCSPC module coupled with a discrete set of single-photon detectors. These detectors are usually arrays of photo-multiplier tubes or single-photon avalanche detectors. Usually, an electronic router assigns each photon detection event to the proper channel. Therefore, it is crucial to reduce the amount of light to limit the possibility of two channel simultaneous detection [48]. There are commercially available TCSPC systems that can have multiple independent channels to overcome this problem, but the cost of these systems rapidly scales up. Moreover, in this technique, a grating or prism disperses the light, further reducing the amount of light that reaches each detector channel. To overcome these methods'
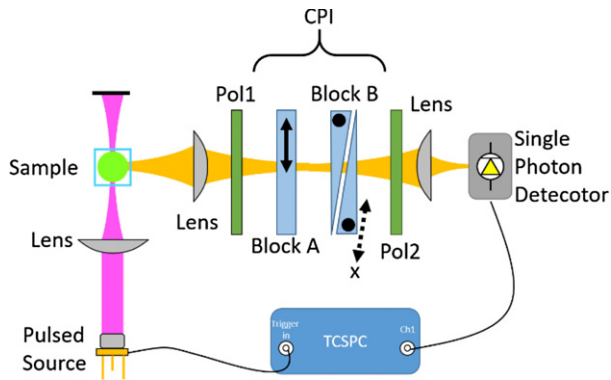
Figure 15. Schematic representation of the experimental setup.

Figure 16. This figure describes the measurement principle to obtain the Starna fluorescence Green polymer's TRES map. (A) 2D interferometric fluorescence map as a function of emission time and position of the interferometer. (B) In solid orange, the fluorescence interferogram, obtained by integrating the map in (A) along the temporal axis. The orange circles indicate the under-sampled interferogram composed of 64 data points. (C) TRES fluorescence map as a function of detection wavelength and emission time, obtained by FT of (A). (D) The cumulative spectrum of (C), obtained by integrating the map along the vertical direction. (E) The semi-logarithmic plot of two vertical cuts of map (C) corresponds with the excitation laser and the prominent emission peak. The orange circles are related to the under-sampled data set.

limitations, we developed a new detection scheme combining a single counting detector and a TCSPC board to record the temporal information and a CPI to measure the spectral one [49].

3.3.2. Experimental setup. Figure 15 schematically represents the experimental setup. A pulsed narrow-band source excites the sample fluorescence. A lens focuses the excitation beam on the sample. A second lens, identical to the first one, is placed at $90°$ with respect to the narrow-band beam to reject, to some extent, the scattered light. The light passes through the CPI and is focused by a lens and made to interfere at the single-photon detector. The single-photon detector was connected to a TCSPC system.

3.3.3. Measurement principle. For each step of the interferometer, the TCSPC system measures a fluorescent decay histogram. The measured decay traces are piled-up together to form an interferometric map $F_L(x, T)$. Here, x and T are the interferometer position with respect to the zero interferometric delay and the emission time, respectively. An FT as a function of the x position retrieves the time-resolved emission spectrum:

$$F_L(f_x, T) = \int_{x_{min}}^{x_{max}} F_L(x, T) e^{-i2\pi f_x x} \, dx, \qquad (20)$$

where, f_x is the spatial frequency and x_{min}, x_{max} are the start and end position of the interferometer scan. All the previously described calibrating procedures are used to convert this map to the final time-resolved emission map $F_L(\lambda, T)$ as a wavelength function. A Jacobian conversion:

$$F_L(\lambda, T) = \frac{F_L(\nu, T)}{\lambda^2} \qquad (21)$$

was applied as a final step to convert from optical frequencies to wavelengths [15].

3.3.4. Results. Figure 16 shows the measured interferometric map $F_L(x, T)$ of the NIST traceable Starna fluorescence Green polymer. The sample was excited by using a picosecond laser diode centered at 440 nm (LDH-P-C-440, Picoquant GmbH). The repetition rate was set to 40 MHz. A variable attenuator attenuated the excitation beam down to
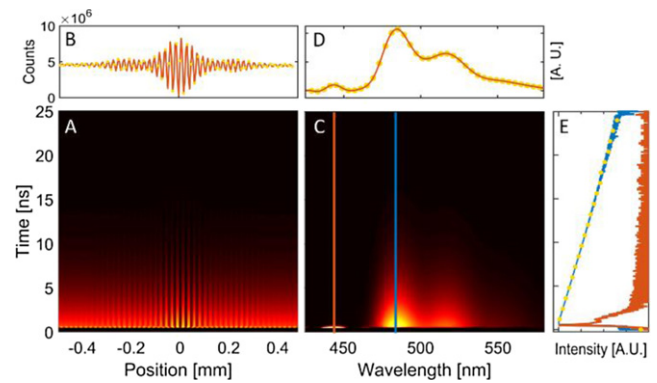
reach a 100 μW power level. A hybrid photomultiplier detector (PMA Hybrid 06, Picoquant GmbH) measured the fluorescence single-photon events. We programmed the CPI (GEMINI, NIREOS s.r.l.) to perform a scan from -0.5 mm to $+0.5$ mm comprising 194 position steps. The maximum and minimum scan positions were selected to include all the residual modulation at the interference signal's tails. A PicoHarp300 TCSPC system (Picoquant GmbH) measures the temporal histograms comprised of 65 536 bins of 4 ps resolution. We set the acquisition time for each histogram to 5 s. We chose a high number of points for visualization purposes to show a nice-looking interference signal. We could have reduced the number of points by more than three times for the selected sample without losing spectral information. The orange circles in (B) and (D/E) sub-parts of figure 16 show the result of this decimation. It is important to note that performing this decimation does decrease the signal-to-noise ratio of the measurement. This decimation was possible by noting that the fluorescence emission bandwidth for the measured dye was limited to a few hundred nanometers. In general, the theoretical minimum number of samples is given by [14]:

$$N = \frac{2(\lambda_{max} - \lambda_{min})}{\Delta\lambda}, \qquad (22)$$

where λ_{max} and λ_{min} are the minimum and maximum wavelength, respectively. $\Delta\lambda$ is the measurement spectral resolution.

It is important to note that further data point reductions are feasible by sampling the interferogram only in positive or negative positions. This is possible by noticing that the interferogram is a symmetric function. Moreover, thanks to the common-path geometry, the zero position (the symmetric point of the interferogram) is known, and

it is accessible with high reproducibility and accuracy. Figure 16(B) displays the interferogram of the fluorescence emission. The interferometric contrast M defined as:

$$M = \frac{I_{\max} - I_{\min}}{I_{\max} + I_{\min}}, \tag{23}$$

where $I_{\max}$ and $I_{\min}$ are the maximum and minimum intensities, peaks at 90% despite the spatially incoherent nature of the emission.

Figure 16(C) shows the sample time-resolved emission spectrum (TRES) as obtained by performing a row-by-row FT. Figure 16(D) shows the cumulative emission spectrum. The sample emission has a maximum at 483 nm and two shoulders at 515 nm and 555 nm, respectively. A small contribution due to the laser excitation is visible at 440 nm. This is due to scattering inside the solid sample. The semi-logarithmic plot of figure 16(E) displays two vertical cut profiles of the TRES map corresponding to the blue and red lines in (C). The red curve corresponds to the scattered laser light and shows a sharp temporal behavior. Its FWHM is around 80 ps highlighting the minimum instrument temporal response. The blue curve corresponds to the peak of the fluorescence emission at 483 nm and shows a monoexponential decay with a time constant of 5.3 ns.

3.3.5. Discussion. The developed setup has several advantages compared to available dispersive techniques based on a monochromator (serial acquisition) or a spectrograph with several detectors (parallel acquisition). Indeed, the presented interferometric technique uses only a single detector, significantly reducing single-photon multichannel detector arrays' technological constraints. In general, single element detectors are faster and more sensitive than their counterparts placed inside a linear array. Indeed, it is a significant technological challenge to manufacture large quantities of fast and sensitive detectors and place them contiguously to employ a grating or prism dispersive effect. This is mainly because these detectors typically require bulky multi-stage cooling systems to reduce spurious dark counts. Furthermore, a trade-off between spectral resolution and spectral range is always present in the parallel approach [50]. Moreover, these spectral parameters can be changed only by changing the physical parts of the instrument. The number of single-photon detectors in a one-dimensional array is limited to a few tens of units, and the cost scales dramatically with their number. The use of multiples detectors requires to use calibrating procedure and known reference samples to compensate for the different efficiencies in the spectral channels. Each detector must be properly synchronized to the others to assure a constant zero time throughout the spectral channels. Using a single-pixel detector, it is possible to use large active areas, greatly enhancing the instrument's sensitivity. Instead, the usable bandwidth of the CPI is very broad and limited only by the transmission of the used birefringent crystals. It is usually restricted only by the employed single-photon-detector spectral responsivity. The spectral resolution can be varied by the user, simply by increasing or decreasing the interferometer's scan range. Dispersive techniques require an entrance slit with a width of a few tens of
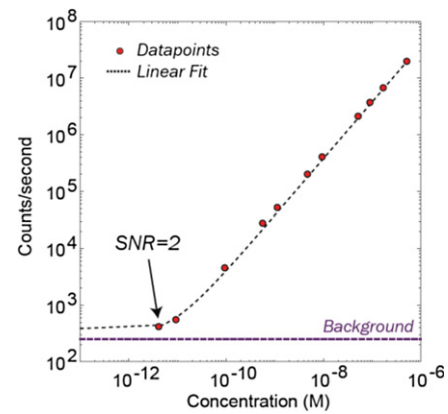

Figure 17. This figure shows the result of the sensitivity test. The background level indicates the number of dark counts while the excitation laser is turned off. The dotted line is a fitting curve highlighting the expected sensitivity behavior. The S/N = 2 value is reached for a remarkable pico-molar concentration level.

micrometers, which affects the light throughput, hence the sensitivity. Instead, the throughput of the CPI is very high since the entrance aperture is large, easily reaching 10 mm, and the light path inside the device is short, down to few centimeters. Moreover, the interferometer's throughput does not depend on the chosen resolution as with dispersive techniques, where one has to reduce the entrance slit accordingly. Generally, the CPI response is spectrally more flat than grating-based devices, which improves the dynamic range of the system.

3.3.6. Sensitivity. To demonstrate the device's state-of-the-art performances, the spectrum of rhodamine B was measured decreasing the concentration down to the instrument's ultimate sensitivity limit. The sample was made by dissolving rhodamine (B) from powder state. This sample was selected because its fluorescence properties such as quantum efficiency, absorbance, and lifetime are well known. In this way, this measurement can serve as a reference for the expected sensitivity using the described instrument. A 532 nm pulsed laser with 235 μW average power was employed. Figure 17 shows the result of this sensitivity test. Remarkably, the fluorescence signal starts to be buried in the dark background only at pico-molar concentration levels.

4. Spectral imaging

Spectral imaging aims to measure the spectrum of the light coming from each point of a scene of interest [51]. This light is generated from an emission, scattering, or reflection process. Analyzing these kinds of measurements, it is possible to obtain physicochemical information and compare and correlate the behavior of different parts of the image composing the scene. A spectral image can be visualized as a three-dimensional data cube (x, y, ω) containing the spectral information about each specific point (x, y) of an image [52].

This large quantity of data contains much redundant information. Therefore, many numerical methods have been developed to extract only meaningful information about an object's properties [53, 54].

This technique has been applied in a wide range of applications such as remote sensing [55, 56], biological imagining [57], land monitoring both in agriculture [58, 59] and in geology [60, 61], in military fields [62] and cultural heritage both for archaeology and conservation of artworks [63–65].

There are many technological ways to measure spectral images. The simpler one is to use a spectrometer to acquire the spectrum for every single point serially. The object or the camera are moved in two dimensions to measure the complete spatial information. This method is known as point scanning or whisk-broom imaging. It is very slow, especially in applications where a high spatial resolution is needed.

Another approach is known as push-broom. It employs a two-dimensional detector to simultaneously acquire spectro-spatial information about a single line on the object plane. The full spectral image is obtained by moving the object or the instrument along a single dimension. This approach has a huge application for industrial process monitoring. Indeed, it is suitable to quickly analyze industrial products on conveyor belts. The main limitation of this approach is related to the use of an entrance slit that is necessary to obtain both spectral and spatial resolution along the moving direction. To increase the spatial or spectral resolution, the slit size must be decreased accordingly. The aperture dimension depends on the specific imager, but it is usually around a few tens of microns, affecting the light throughput.

The wide-field approach employs a spectral filter to directly acquire many two-dimensional images of the entire scene at each wavelength of interest. Usually, this filter is an acousto-optic filter or a liquid crystal tunable filter, or simply a filter wheel [66]. However, many technical issues prevent the widespread use of this approach. They are all linked to the difficulties in designing and producing, with the available technologies, a variable spectral filter with a good transmission in a broadband spectral range and to achieve a high spectral resolution [67].

4.1. Fourier transform spectral imaging

Recently, an alternative spectral imaging method has been developed based on FT spectroscopy principles [49]. This approach combines a monochrome two-dimensional sensor measuring the scene's spatial properties and an interferometer, used to achieve the spectral resolution on each point of the image.

As discussed in the introduction, using an interferometer instead of a dispersive monochromator carries several advantages in terms of throughput, versatility, and accuracy. Additionally, the spatial resolution can be adjusted independently from the spectral resolution. FT spectral imager acquires continuous spectra for each pixel, and they are not limited to only discrete wavelengths like in dispersive technology by using a filter wheel.

In most spectral imaging applications, the light comes from spatially incoherent sources, such as the light reflected from an object or emitted following a fluorescence decay. For this reason, the interferometer employed in the Fourier-transform-based imaging systems must maintain a high degree of coherence among all different electromagnetic waves that interfere at a single pixel of the bi-dimensional detector. This is an essential property to achieve a good interferometric contrast, hence the visibility of the interference fringes and consequently a good spectral quality. Moreover, the interferometric stability between the interfering fields must be kept down to a 1/10 fraction or better than the optical cycle. This is especially hard in the visible and ultraviolet spectral regions, where an attosecond-level accuracy of the delay is in general requested.

There are two ways to measure the light's interference signal coming from each point of the image. In the static approach, an easily manageable interferometer with no moving part is used. A spatial interferogram is measured for each scene point by using one dimension of the bi-dimensional detector. The complete measurement of the spectral image is performed similarly to the push-broom method by inducing a relative movement of the instrument with respect to the scene [68]. This approach, as the push-broom method, is desirable for industrial or airborne remote sensing applications. However, they require a large enough pixel density along the detector dimension used to sample the spatial interferogram and a large enough detector to achieve a good resolution. This imposes several constraints on the used detector. Moreover, this approach tends to favor the use of a small pixel area, decreasing the collected light and, consequently, the instrument's sensitivity. In the non-static approach, the interferometric delay is mechanically changed and a complete interferogram is recorded for each pixel of the two-dimensional sensor. In this method, there is no need for any relative movement between the camera and the scene. Instead, the sample must be static for all the time needed to complete the interferometer scan, making this method particularly suited for a stationary scene such as measuring artworks. Both Michelson's and Mach–Zehnder interferometers were used for this task, but they required particular attention in stabilizing the device, especially for the visible spectral region [69].

For this reason, new ultrastable interferometers have been developed in recent years to bring some of the advantages of FT spectroscopy down to the ultraviolet and visible spectral ranges. All these devices employ birefringence, either dynamic, such as the one induced by applying a static voltage across liquid crystals, or static, the one of natural crystals [70–72]. These devices are extremely compact and insensitive to mechanical vibrations thanks to their common-path geometry. However, liquid crystals are quite sensitive devices since their features are strongly dependent on the working temperature. Therefore, they need accurate calibration and active closed-loop temperature control to achieve long-term spectral response stability. Moreover, they are spectrally limited to a few hundred nanometres spectral bandwidth, usually limiting them to the visible spectral range (400–750 nm) or in near infrared range (750–1100 nm). They are easily damaged by long term infrared radiation exposure. Therefore, proper short-pass filters need to be used to increase their working lifetime. However, they have fast switching time between different wavelengths and a good spectral uniformity across the image field, making them ideal for certain applications.

In recent years, many birefringent crystal-based interferometers have been used in combination with two dimensional sensors to acquire spectral images. In this kind of devices, a birefringent optical element is moved to change the path length difference between the ordinary and extraordinary polarization components. The interference signal is measured for each point of the scene of interest by a single pixel of a two-dimensional detector. These FT-based imagers typically employ a Wollaston or a Savart prism [73, 74]. The transparency and birefringence of the employed crystals are very broad. It typically covers from the visible to the longer edge of the short-wave infrared spectral region. Therefore, their spectral range is mainly limited only by the limited bandwidth of the employed detector.

However, these prisms tend to disperse the interferometer replicas chromatically. This, in turn, decreases the interferometric modulation and the visibility of the interference fringes in the detector plane. Indeed, the employed prisms divide the light into two orthogonally polarized replicas. These are angularly separated and need to be combined again by another optics (i.e., a lens) before the imaging detector. The two light replicas interfere at the detector coming from different directions. Therefore, also the wavefronts of the two beams are inclined accordingly. This causes a loss of the interferometric modulation at the detector that reduces the signal to background ratio. Moreover, the used prisms angularly separate the light's spectral components, which further reduces the interferometric modulation at the detector. Indeed, the same spectral component of the two orthogonally polarized replicas impinges onto a slightly different camera position, thus reducing the interferometric signal's modulation.

4.2. Experimental setup

The previously described CPI was used to assemble a spectral imaging system. This interferometer overcomes the Wollaston and Savart prism-based imager's limitations, providing negligible chromatic dispersion and small geometrical separation between the interfering replicas. This leads to a high degree of coherence at each pixel and a strong interference modulation.

It is important to note that the air gap between the two wedge-shaped blocks introduces chromatic dispersion in the two replicas. However, this effect can be reduced to a negligible level by decreasing the gap width (down to 1 mm) and by compensating the effect with the optical alignment of the block A and B. Figure 18 shows the experimental setup. The CPI is placed in between the object plane and the objective of a monochrome camera. Each pixel of the camera measures the interference signal corresponding to the light coming from a single point of the scene. In this scheme, an uncollimated beam passes through the interferometer. However, the CPI works equally well for collimated and uncollimated light thanks to its common path nature and the very short path inside the interferometer. Therefore, other optical elements can be inserted in between the CPI and the sample. This is especially beneficial in applications requiring high versatility in selecting the angular field of view of the camera, such as remote sensing and microscopy [75, 76].
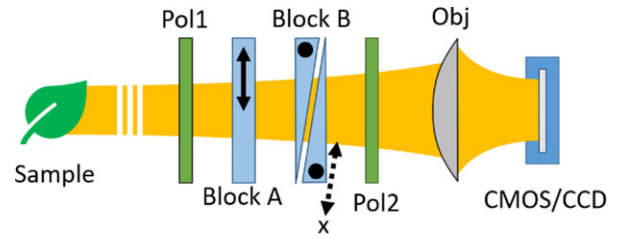

Figure 18. Experimental setup of the developed spectral imager.

4.3. Fringe visibility

To estimate the fringe visibility in the developed imaging system, we will evaluate the employed CPI's behavior for a generic ray propagation direction. To simplify the mathematical description, we can model the interferometer as two birefringent blocks with crossed optical axes. Considering figure 19(A), block B represents the wedge pair, whereas A is the fixed plate. We will not consider the air spacing and the corresponding crystal–air interface refractions between the two wedges in this treatment. This system can be applied to generate delayed replicas of fields propagating with a general incident angle α. In the following description, the phase delay ψ_T of the interferometer is defined as the relative phase delay between the two replicas of a ray propagating at $\alpha = 0$. This direction corresponds to a light beam propagating normally to the wedge surface. Considering a ray passing through the imaging system with an angle α with respect to the normal direction. We obtain that the vertically and horizontally polarized components accumulate a relative phase shift ϕ. Panel (c) of figure 13 plots this phase as a function of α, when $\psi_T = 0$. In this condition, both plates have the same thickness L. The phase difference ϕ is evaluated for a wave at $\lambda = 600$ nm in α-BBO blocks with $L = 2.4$ mm. The incidence angle strongly affects the phase difference, which, in turn, impacts fringe visibility. The interferometer placed in the imaging system generates, for each generic ith ray, two phase-delayed ($\phi_T + \psi_i$) replicas. We can write their superposition as:

$$E_i = A_i \cdot [\cos(\omega t) + \cos(\omega t - \psi_T - \phi_i)]. \quad (24)$$

Where we consider a single angular frequency for simplicity and ψ_T and ϕ_i are the relative phase delays, as follows:

- ψ_T is introduced by varying B block's thickness; $\psi_T = 0$ when the two blocks (A and B) have the same thickness.
- ϕ_i depends on the propagation direction as shown in figure 19(C).

In an imaging system, the light emerging from each scene's point can be represented as a bundle of rays traveling through the interferometer and the imaging optics into the corresponding pixel at the image plane. This is schematically represented in figure 19(B) with all the key parameters defining the system. For each point O in the object plane, it is possible to define two marginal rays with angle α_1 and α_2. Without considering chromatic and spherical aberrations, each beam starting from the O point and having an angle between the two marginal angles is focused on the same point I in the image plane. Analogously,
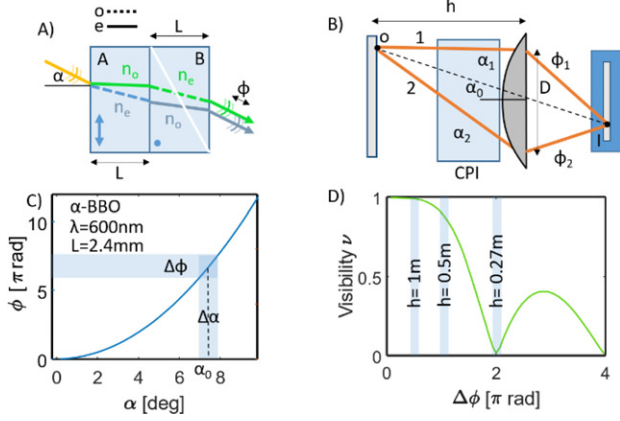
Figure 19. (A) Schematic representation of the model used in the to estimate fringe visibility. The blue line indicates the path of the vertically polarized component inside the interferometer. The green line indicates the horizontally polarized component. The line is drawn in solid or dotted style for the ordinary rays and extraordinary rays, respectively. The blue arrows and dots indicate the optical axes of the A and B blocks. (B) Imaging scheme of the employed spectral imager with all the key parameters defining the system. (C) The blue curve shows the relative phase between the two replicas as a function of the incidence angle α. The blue area is the phase change as a function of the incidence angle. (D) The visibility plot as a function of the relative phase range $\Delta\phi$ is shown in green. The blue areas correspond with the relative phase ranges parameters corresponding to several object/aperture distances ($h = 1$ m, $h = 0.5$ m, and $h = 0.27$ m).

we can define the marginal relative phase difference as ϕ_1 and ϕ_2. Therefore, for each specific phase delay ψ_T, the superposition of all these rays coming into a single pixel position J in the image plane, where the two-dimensional sensor is placed, can be written as:

$$E_J(T) = \sum_i E_i = \sum_i A_i \cdot [\cos(\omega t) + \cos(\omega t - \psi_T - \phi_i)]. \tag{25}$$

The signal intensity at the pixel position is $\|E_J(T)\|^2$, and it depends on the distribution of phase shifts ϕ_i. The interferometric modulation or visibility ν is plotted in figure 19(D) as a function of the phase range $\Delta\phi = \phi_1 - \phi_2$, where ϕ_1 and ϕ_2 are the relative phase differences between the interfering replicas for the marginal rays as depicted in figure 19(B). This curve was numerically computed considering a worst-case scenario in which the amplitude A_i is constant and ϕ_i is uniformly distributed in the range $\Delta\phi$. The visibility is calculated by numerically scanning ψ_T in the neighborhood of $\psi_T = 0$ [77]. When the phase-shifts ϕ_i of the ray bundles range from ϕ_1 to ϕ_2, it is possible to show that the interferometer zero path-difference, which is the center of the interferogram, is shifted at $\psi_0 = \langle\phi\rangle$, where $\langle\phi\rangle = (\phi_2 - \phi_1)/2$. Therefore, the interferometric delay is not uniform in the image field. Indeed, the interference fringes follow a hyperbolic pattern. In this framework, we can estimate the expected fringe visibility of the described spectral camera. As shown visually in figure 19(B) and graphically in figure 19(C), the phase range is strictly related to the ray's angular spread coming from a point O in the object plane.
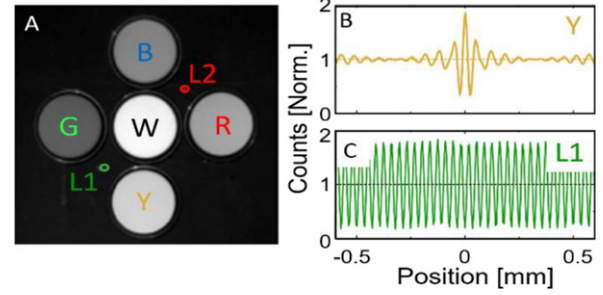

Figure 20. (A) Single capture of the test sample. The R, G, B, Y, and W labels correspond to the red, green, blue, yellow, and white reflectance standards. L1 and L2 indicate the laser point positions for the 532 and 635 nm laser lines, respectively. (B) Interference signal corresponding to a pixel in the Y area. (C) Interferogram corresponding to one pixel in the L1 region of the test sample.

Mathematically, this angular range is given by:

$$\Delta\alpha = \|\alpha_1 - \alpha_2\| \approx \arctan \frac{D/h}{1 + \tan^2 \alpha_0} < \arctan(D/h), \tag{26}$$

where α_1, α_0 and α_2 are the top, middle, and bottom ray angles, respectively, as shown in figure 19(B). D is the aperture diameter, and h is the distance between the object plane and the aperture of the spectral imager. Figure 19(B) shows that the phase spread $\Delta\phi$ for a given angular range $\Delta\alpha$ is higher for the points located at the edge of the field of view, hence with higher α_0 values. The maximum α_0 value for the system used in this experiment was around 7.7°.

The dotted lines in figure 19(C) highlight the visibility values calculated for the different object-to-camera distances. This computation is performed for the worst-case scenario. The point is at the edge of the field of view. Very high visibility of more than 85% for all the field of view is reached for an object located more than 0.5 m away from the camera aperture, demonstrating the good interferometric quality of the designed system.

4.4. Results

We validated the spectral camera (HERA, NIREOS s.r.l.) by measuring the spectral image of a test scene shown in figures 20(A) and (B). This scene was composed of 4 colored circular spectral standards whose reflectances are tabulated (green, blue, red, yellow, G, B, R, and Y). In addition, a white reflectance standard was placed in the center of the scene. This white element has a flat spectral reflectivity of 98.3% from 300 to 2500 nm. These circular standards were manufactured by Labsphere Inc., North Sutton, USA.

To test the developed system's spectral resolution, we inserted two laser spots at different wavelengths in the image at points L1 and L2. The emission wavelengths of these lasers are $\lambda = 532$ nm and $\lambda = 635$ nm, respectively. The bandwidths of these laser lines are below 0.37 THz.

A broadband 150 W xenon lamp was used to illuminate the test sample. We opened the variable iris of the camera objective to its maximum, corresponding to an $f/1.8$
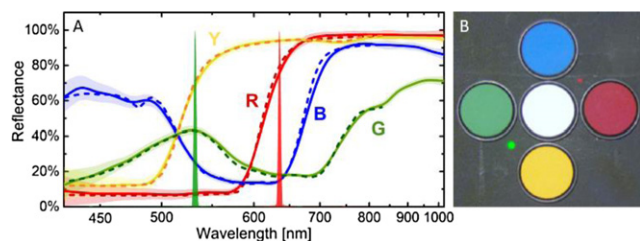
Figure 21. (A) Comparison between the reflectance spectra of the standards as measured with the developed spectral imager as solid lines and the tabulated ones as dotted curves. The colored area shows each spectrum's error bar as measured by computing the spectrum standard deviation of neighboring pixels. The green and red peaks refer to the 532 and 635 nm laser spots. (B) shows a projection of the spectral data cube into the RGB space as computed for a D65 standard illuminant (CIE 1964).

aperture. Finally, we programmed the interferometer to perform 400 evenly spread steps in a 2 mm scan range around the interferometer's zero position. We acquired an image for each position of the interferometer. The integration time of each image was set to 25 ms.

The total acquisition time was below 30 s, comprising motor movement and image data transfers to the computer. It is important to note that the interference signal was sampled well above the Nyquist condition only for visualization purposes. Therefore, the acquisition time can be significantly decreased. Indeed, the position step size of the interferometer used for this measurement was 5 μm. This value corresponds to a delay of 0.25 fs at 600 nm, 1/8 of its optical cycle. Figures 20(B) and (C) represent the interference signals for two pixels located in the sample's Y and L1 regions, respectively. A central burst dominates the yellow curve, and the oscillations decay rapidly increasing the interferometer's position, while the green interferogram is a long-lasting sinusoidal function. This behavior underlines the different coherence times for the light coming from the two points in the object plane. The two interferograms' interferometric modulation values are 86.5% and 84%, for the Y and L1 pixels, respectively. This visibility could be increased by decreasing the variable aperture dimension. However, the light throughput of the system is decreased in the same way. The optimal aperture size depends on the scene type and the desired depth of focus. It is important to note that the visibility of the interferogram is a crucial parameter for instrument sensitivity [78].

Figure 21(A) shows the normalized spectra of the green and red laser diode spots. These spectra were extracted from a long-range measurement. The positions of these spectral peaks were used to calibrate the interferometer according to the previously described procedure [8, 35, 36]. The bandwidth of these laser lines was used to measure the spectral resolution of the device at the two corresponding wavelengths. The resulting bandwidth of the 635 nm laser spectrum is $\approx$ 4 nm and is 1/150 of the total spectral range of the camera. The 535 nm laser linewidth is shown to be around 3.3 nm.

To validate the system, the reflectance spectral image of the test sample was measured. The light source was placed at 3 m

distance from the object to produce uniform illumination of the field of view both in intensity and spectral features. To obtain the reflectance data, a uniform white Lambertian surface was measured. This sample has an average reflectance of 95% in the working spectral range. The spectrum related to each pixel of the test sample's spectral image was normalized by the corresponding one of the Lambertian measurements. This procedure normalizes both intensity and spectral unevenness in the field of view. The absolute reflectance image was computed by normalizing this image to the know white reflectance standard's reflectance value. The reflectance spectra measured with the developed spectral imager for the red, blue, green, and yellow standards are plotted in figure 21(A). The dashed curves show the tabulated spectra for the reflectance standards. To compare the measurement with these reflectance standards' certified spectra, we evaluated the mean standard deviation of the difference between the measured and tabulated spectra of each standard. The maximum deviation is around 2.18% for the blue spectral standard. This value is probably due to the low sensitivity of the used camera in the blue spectral region. Notably, the spectra's spectral range as measured with the developed instrument was broader than the tabulated one. Only the matching region of the spectral axis for the two measurements was considered in this comparison. Figure 21(B) shows the projection of the reflectance spectra in the RGB space. The image projection was computed by considering a D65 illuminant (CIE 1964).

The high sensitivity of the described spectral imager is ideal in low light conditions. For this reason, it has been used in cultural heritage where low illumination levels are usually required to avoid damaging artworks [79, 80], and also in fluorescence measurements [80].

5. Circular dichroism

Optical activity is an intrinsic optical property displayed by chiral molecules, i.e., those not superimposable to their mirror image. Almost all-natural products, biomolecules, and synthetic drugs are chiral. Chirality plays a fundamental role in many biological, chemical, and physical processes, such as catalytic reactions and drug binding to proteins. Determining the handedness of chiral molecules is extremely important for fundamental biochemical studies as well as for applications in the agricultural, pharmaceutical, and food industries. Recently, several efforts have been invested in trying to realize time-resolved optical activity experiments.

If successful, this will open a new paradigm in stereochemistry, allowing researchers to gain mechanistic insights into ultrafast structural rearrangements associated with fundamental biomolecular functions such as light-driven isomerization, ring-opening, and unidirectional rotary motors. A straightforward configuration for the broadband measurement of molecules' optical activity is presented in the following sections. This approach combines time-domain detection with heterodyne amplification. Most importantly, the presented device performs equally well with incoherent light and broadband ultrashort light pulses, paving the way to measurements of transient optical activity changes on the femtosecond

timescale. This method relies on the previously described CPI. This approach allows the simultaneous detection of both the circular dichroism and circular birefringence spectra of chiral compounds. Notably, the presented device is drastically simplified compared to conventional spectropolarimeters since it dispenses with monochromators, photo-elastic modulators, and lock-in amplifiers.

5.1. Time-domain measurement of optical activity by a CPI

The chirality of molecules has a huge influence on many biological mechanisms such as enantioselective catalytic reactions or binding of drugs with the target biomolecules [81]. The distinction of a chiral molecule from its corresponding enantiomer and the identification of their handedness are extremely important. Measurements of the chirality of samples through optical or chemical techniques are routinely done in chemical and pharmaceutic companies. The optical methods to measure chirality are based on the measurement of the so-called optical activity [82] or optical rotation. Namely, the ability of a sample to interact with polarized light changing its plane of polarization. This phenomenon can be distinguished in circular dichroism and circular birefringence. The first one is the difference in the absorption between left and right circularly polarized light. As the name suggests, the latter is a difference in the refractive index of a material interacting with the two-light handedness. These physical entities are of particular interest for studying bio-polymers ranging from proteins to nucleic acids such as DNA and RNA, especially in the ultraviolet spectral range. Circular dichroism spectroscopy is a powerful tool for structural studies and can distinguish between α-helix, β-sheet, and random coil conformations of proteins, determine their secondary structure content, monitor their stability, and study their folding processes [83, 84]. The concept of chirality has also been recently extended to plasmonic systems, exploiting single nanostructures' handedness or their spatial arrangements, showing the potential to increase detection sensitivity thanks to the enhanced light–matter interaction [85].

Considering light–matter interaction processes, a linearly polarized electromagnetic field passing through an achiral sample generates an oscillating material polarization. This creates a response electromagnetic field called achiral free induction decay. This field is superimposed to the input light, and their interference generates linear absorption and refraction. In addition to the achiral free induction decay field, a chiral sample responds to light propagation generating a low-intensity field with a perpendicular polarization with respect to the incoming light. This field is called free induction decay or, more precisely, chiral free induction decay. This small field superimposing to the incoming light changes the polarization state of the beam. In general, this effect leads to a rotation of the polarization plane and to the conversion from a linearly polarized light beam to an elliptical one [86, 87].

By measuring these effects, it is possible to retrieve information on the chiral properties of a sample. However, the chiral free induction decay is commonly several orders of magnitude less intense than the incoming light. Therefore, it is hard to measure its effect on the incoming beam.

In the visible, this is typically performed by a circular dichroism spectrometer, also known as a spectropolarimeter. In this device, the light coming typically from a broadband source is filtered employing a monochromator. The resulting single-wavelength light is then periodically and alternatively converted into a right or left circularly polarized beam. This is done very fast, typically a few thousands of times per second. The light passes through the sample, and a detector measures it. The chiral sample absorbs the two light polarization states differently, so the measured signal is composed of a strong constant background, the light transmitted by the sample superimposed to a small periodic signal with the same frequency of the imposed modulation. Then, this tiny periodic signal is extracted with a lock-in amplifier. This device can extract a sinusoidal signal with a known frequency from a constant background, even if the relative intensity between the two is different by several orders of magnitude. The amplitude of this signal is measured by varying the excitation wavelength, and the result is the circular dichroism spectrum, highlighting the absorbance difference between the two-circular state of the excitation light as a function of the wavelength. It is important to note that this technique can extract information only on the circular dichroism and not on the circular birefringence properties of the measured sample. This information is typically computed employing a Hilbert transformation, following the Kramers–Kronig relationship [88, 89].

In the infrared spectral region, the measurement is typically performed by employing FT spectroscopy's advantages. This is performed by replacing in the spectro polarimetric system the monochromator with a double beam amplitude division interferometer, typically of a Michelson's type. In this temporal domain technique, it is also possible to extract the circular birefringence spectrum by measuring with the addition of a polarizer between the sample and the detector [90]. These devices based on a lock-in amplification scheme and photo-elastic modulators are the only available methods in the market and are widely spread in the scientific and industrial fields. However, they are delicate, expensive, and bulky machines requiring frequent calibrations.

For these reasons, new approaches have been developed for measuring the circular dichroism spectra of samples. These are mainly based on the use of a double-beam polarization division interferometer. In these interferometers, the light propagates in the two arms with an orthogonal polarization [91]. Ragunathan *et al* [92] and Polavarapu *et al* [93] pioneered using such a device to record vibrational circular dichroism spectra. In these kinds of devices, the relative delay between the two orthogonally polarized beams is changed by adjusting the two arms' path length difference. Depending on the relative delay, the superposition of these perpendicular fields creates a beam with a variable polarization state. Indeed, we can note that the output beam polarization is linear when the paths in the two arms match. Then by changing the delay, the polarization state is transformed continuously to an elliptical, circular, again elliptical and orthogonal linear polarization, respectively. Finally, by increasing even further the delay, the polarization returns to its original state and this behavior is repeated in a periodic fashion. In this way, the light state is changed whereas the overall

light intensity is constant, because perpendicularly polarized components do not interfere. If now a chiral sample is placed inside the device, it rotates the polarization state according to the generated free induction decay, and an interferogram can be recorded at the output employing the detector. Then, the circular dichroism spectrum can be retrieved using a Fourier transformation.

Another approach based on spectral interferometry was proposed by Rhee *et al* [94–96]. A Mach–Zehnder interferometer was set to produce a strong replica with a vertical polarization and a horizontal polarization one with a lower intensity. Instead of scanning the interferometer delay and recording the signal in the time domain, the delay was fixed and the light transmitted by the sample was dispersed on a spectrometer after passing through a linear polarizer. This device, called also analyser had a very high extinction ratio and was aligned along the horizontal direction. In this configuration, the chiral free induction decay field with horizontal polarization, generated by the interaction of the vertical polarized replicas with the chiral sample, interferes with the horizontally polarized replica, acting as a local oscillator (LO). The complex chiral signal $S_{\mathrm{H}}(\omega, \tau)$ is computed by means of a Hilbert transform following the Kramers–Kronig relations and an achiral reference signal $S_{\mathrm{V}}(\omega, \tau)$ is measured with the last polarizer oriented along the vertical direction. The circular dichroism and circular birefringence spectra can then be calculated with the following formula [97]:

$$\frac{S_{\mathrm{H}}(\omega, \tau)}{S_{\mathrm{V}}(\omega, \tau)} = \mathrm{CB}(\omega) + \mathrm{iCD}(\omega), \qquad (27)$$

where $\mathrm{CB}(\omega)$ and $\mathrm{CD}(\omega)$ are the circular birefringence and circular dichroism spectra, respectively.

These promising interferometric techniques were used to measure spectra with a good sensitivity, but they are mainly limited by the high interferometric stability required. This is because a double beam interferometer is very sensitive to environmental perturbations such as vibrations. Indeed, a fluctuation of the path length difference between the two arms of the interferometer by more than a tenth of the wavelength is sufficient to destroy the interference, hence the measurement. This problem is partially reduced in the infrared regions looking at the vibrational circular dichroism of samples. This is because by increasing the wavelength, the stability requirements are reduced. To work in the visible range, these double-beam interferometers require an active stabilization loop or a single shot detection of $S_{\mathrm{V}}(\omega, \tau)$ and $S_{\mathrm{H}}(\omega, \tau)$ using a double-channel spectrometer [98, 99].

In the following sections, a new approach will be presented based on the use of a common-path birefringent interferometer. The spectral range of this approach is only limited by the birefringence and transparency of employed birefringent crystals. By a proper choice of the material, it is possible to work from the ultraviolet to the mid-infrared spectral region, from 200 to 10 000 nm, respectively. The interferometer is adjusted to create two orthogonal replicas of the excitation light. The relative intensity is tuned through an entrance polarizer to produce a strong vertical replica and a weaker horizontal one. The first is used to generate a horizontally polarized chiral
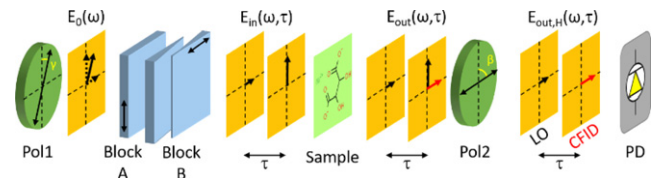

Figure 22. This image schematically represents the working principle of the developed FT spectropolarimeter. The first polarizer marked as P1 is rotated at a small angle γ with respect to the vertical. It creates a linearly polarized light field that is indicated in the figure as $E_0(\omega)$. The beam passes through the CPI. Consequently, the two perpendicular polarization components are delayed by τ creating an electromagnetic field $E_{\mathrm{in}}(\omega, \tau)$. The vertical component interacts with the chiral sample, to generate a horizontal free induction decay field, indicated in the figure as CFID with a red arrow. The less intense horizontal polarization field acts as a LO. The exit polarizer P2 acts as an analyzer and its transmission axis is directed with an angle $\beta = 90°$, selecting the horizontal part $E_{\mathrm{out,H}}(\omega, \tau)$ of the field after the sample. A photo-detector measures the interference signal of the LO and the chiral free induction decay field as a function of the interferometric delay. An FT of the signal as a function of τ provides the circular dichroism and birefringence spectra.

free induction decay. The latter is used as a LO enhancing the chiral free induction decay signal. The two horizontally polarized replicas are selected utilizing a polarizer. The interference signal between the two fields is recorded employing a single-pixel detector. The circular birefringence and circular dichroism spectra are computed through an FT procedure. The working principle was demonstrated both for incoherent thermal light and with a broadband supercontinuum laser source [100]. This can lead in the future to the measurement of time-resolved optical activity on the femtosecond and picosecond temporal regime.

5.2. Measurement principle

A schematic representation of the experimental setup is shown in figure 22. The entrance polarizer P1 is rotated to have a transmission axis oriented at γ with respect to the vertical direction. This polarizer creates a linearly polarized electromagnetic wave along the transmission axis.

This field can be represented as the superposition of two replicas, one oriented along the vertical direction and the other along with the horizontal one. A variable temporal delay τ separates these two fields by propagating inside the CPI. The optical activity is a linear optical property. Thus we can use the superposition principle to describe the measurement principle. Indeed, it is convenient to decompose the broadband excitation light into single monochromatic waves. Each one can be identified by an angular frequency ω and an amplitude $E_0(\omega)$. Using Jones calculus, we can write the electric field after the CPI as [101]:

$$E_{\mathrm{in}}(\omega, \tau) = E_0(\omega) \begin{pmatrix} \sin \gamma \\ \cos \gamma \, \mathrm{e}^{\mathrm{i}\omega\tau} \end{pmatrix}, \qquad (28)$$

where $\omega\tau$ is the phase difference between horizontal and vertical components introduced by the interferometer, and τ is their relative delay. In the framework provided by the Jones calculus, the propagation inside a chiral sample can be described as

a simple matrix multiplication, therefore the electric field after the sample is:

$$E_{\text{out}}(\omega) = M_{\text{chiral}} \cdot E_{\text{in}}(\omega), \tag{29}$$

where M_{chiral} is the Jones matrix describing a chiral medium with a length L. In the limit of a weak free induction decay field with respect to the incoming excitation light, this matrix can be written as [102]:

$$M_{\text{chiral}} \approx 10^{-\alpha/2} \, e^{-i\rho} \begin{pmatrix} 1 & \text{CB} - \text{iCD} \\ -\text{CB} + \text{iCD} & 1 \end{pmatrix}, \tag{30}$$

where $\alpha = (\alpha_{\text{LCP}} + \alpha_{\text{RCP}})/2$ is the mean absorbance of a sample, hence the one it would have with a linearly polarized light beam. ρ is defined to be $\rho = nL\omega/c$, where $n = (n_{\text{LCP}} + n_{\text{RCP}})/2$ is the mean refractive index and c is the speed of light in vacuum. The optical rotation is defined as:

$$\text{CB} = \frac{(n_{\text{LCP}} - n_{\text{RCP}})L\omega}{2c} \tag{31}$$

and the ellipticity expressed in radians is:

$$\text{CD} = \frac{(\alpha_{\text{LCP}} - \alpha_{\text{RCP}})\ln(10)}{4}. \tag{32}$$

A second polarizer P2 is oriented with the transmission axis along the horizontal direction. This is highlighted in figure 22 where the transmission axis is represented with an angle $\beta = 90°$. Therefore, the polarizer extracts only the horizontal component of the field after the sample, obtaining:

$$E_{\text{out,H}}(\omega, \tau) = E_0(\omega)10^{-\alpha/2} \, e^{-i\rho} \cdot$$
$$\cdot \left[\sin\gamma + (\text{CB} - \text{iCD})\cos\gamma \, e^{i\omega\tau} \right]. \tag{33}$$

We can note that the equation (33) is the superposition of the chiral free induction decay field with the horizontal component of E_{in} after the propagation inside the sample. This last field acts as a LO enhancing the small chiral signal. After the last polarizer, the transmitted light intensity is measured by a color-blind detector as a function of the interferometric delay τ. The measured signal is the chiral interferogram and can be computed considering the effect of each monochromatic component as:

$$I_{\text{chiral}}(\tau) = \int \| E_{\text{out,H}}(\omega, \tau) \|^2 \tag{34}$$

by neglecting the weak chiral free induction decay intensity, we obtain:

$$I_{\text{chiral}}(\tau) = \int \mathrm{d}\omega \| E_0(\omega) \|^2 10^{-\alpha(\omega)} \cdot$$
$$\cdot \left[\sin^2\gamma + \sin 2\gamma \cdot (\text{CB}(\omega)\cos(\omega\tau) - \text{CD}(\omega)\sin(\omega\tau)) \right]. \tag{35}$$

In this last formula, we can recognize a term proportional to the LO's intensity and a more interesting mixing term between the LO and the chiral free induction decay field. The latter is the term describing the self-heterodyne amplification process.

The circular birefringence and dichroism spectra can be retrieved by taking the chiral complex spectrum's real and imaginary parts. This spectrum is the FT of the chiral interferogram. A calibration process is necessary to calculate the absolute values of the signal. This can be accomplished by measuring the resulting signal with the same detector after tilting the second polarizer by an amount $\beta_{\text{cal}} = 45°$. In this configuration, the vertical and horizontal components generated by the CPI interfere at the detector obtaining the calibration interference signal:

$$I_{\text{cal}}(\tau) = \int \mathrm{d}\omega \| E_o(\omega) \|^2 10^{\alpha}(\omega) \cdot$$
$$\cdot \frac{1}{2} \left[1 + \sin(2\gamma)\cos(\omega\tau) \right] \tag{36}$$

the light intensity, sample absorbance, and dependence on the polarizer angle cancel by taking the ratio of the FTs of the chiral and calibration interferograms. Consequently, we obtain the circular dichroism spectrum as:

$$\text{CD}(\omega) = -\frac{1}{2} \Im \left(\frac{FT\left[I_{\text{chi}}(\tau) \right]}{FT\left[I_{\text{cal}}(\tau) \right]} \right) \tag{37}$$

and the circular birefringent spectrum as:

$$\text{CB}(\omega) = \frac{1}{2} \Re \left(\frac{FT\left[I_{\text{chi}}(\tau) \right]}{FT\left[I_{\text{cal}}(\tau) \right]} \right). \tag{38}$$

These equations remain valid even if the absolute value of τ is not known in the experiment. This is the case when the position of the CPI corresponding to the zero optical path difference is not precisely identified. In such a case, the FT of $I_{\text{cal}}(\tau)$ can have an imaginary component.

We can note that the equations (37) and (38) are similar to the equation (27). This last equation was essential to calculate the circular birefringence and dichroism spectra with the spectral interferometry approach developed by Rhee *et al* [94]. However, the method presented in this section directly measures the complex optical activity spectrum. Instead, the setup developed by Rhee *et al* measures only non-complex signals, and the complex signals are indirectly computed by processing techniques based on the Hilbert transform. Being an indirect method, it might be more sensitive to experimental noise problems.

The optical activity signal components are dependent on the chiral interferogram as described by the equation (35). This signal is the sum of two arguments. The first one is proportional to $\sin^2(\gamma)$, and it is not dependent on the interferometric delay, so it introduces a constant offset. The other one is the mixing term which is proportional to $\sin(2\gamma)$, and it is dependent to τ, and it is the only term describing a pure interference process. The chiral signal's interferometric contrast is always less than unity and is in general proportional to $\cot(\gamma)$. Therefore, high values of the angle γ result in a better heterodyne amplification factor, hence a larger fringe amplitude, but it increases the offset, decreasing the interferometric contrast. The opposite is true when the value of the γ angle is decreased. The interferometric contrast is always a key factor to have a good sensitivity because of the limited dynamic range of the acquisition system and shot noise.
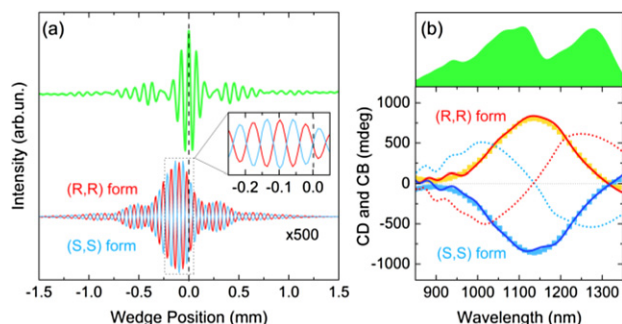
Figure 23. The top part of figure (a) displays the calibration interferogram corresponding to the broadband source light transmitted by the sample (green curve). It was measured with the second polarizer P2 oriented along a direction $\beta = 45°$ with respect to the vertical axis. In blue and red solid lines, the chiral interferograms are shown as measured with the first polarizer oriented at $\gamma = 4°$ of the two enantiomers of nickel tartrate. The measurements were performed with a 310-lumen halogen lamp. The single interferogram measurement time was 5 s. The interferogram is the average of ten interferometer scans. The top part of figure (b) displays the corresponding spectrum of the calibration interferogram shown in green in figure (a). The bottom part of figure (b) contains the circular dichroism and birefringence spectra as solid and dotted lines, respectively. This is done for the (R, R)-form (red curves) and (S, S)-form (blues curves) enantiomers of nickel tartrate. The yellow and blue circles are the circular dichroism spectra as measured with a common dispersive spectropolarimeter.

5.3. Results

The developed spectropolarimeter was used to perform several measurements on a sample made by dissolving nickel tartrate in pure water, reaching a concentration of 120 mM. The interferogram measured with the second polarizer set at $\beta = 45°$ is shown in figure 23 as a light green solid line.

It corresponds to the calibration interferogram $I_{cal}(x)$, where x is the wedge position with respect to the zero position of the interferometer.

Figure 23(b) displays the spectrum of the broadband source light as transmitted by the sample. This spectrum was retrieved by doing an FT along the wedge position axis and performing the spectral calibration process described previously with a set of known interferential filters. We can note that the spectrum shows an evident dip at 1150 nm. This is correspondent to the d–d transition absorption peak. In the bottom part of figure 23(a) two interferograms are shown as blue and red solid curves. These signals were acquired with the second polarizer set at $\beta = 90°$, thus in the chiral measurement configurations. They correspond to the (S, S) and (R, R) forms of the chiral sample, respectively. Notably, the two signals are mirrored with respect to the horizontal axis. The two are significantly shifted with respect to the zero position of the interferogram. The reason for this shift is clearly identifiable by looking at the equation (35). Indeed, the interferogram is a superposition of a sinusoidal and cosinusoidal function with a different amplitude proportional to the circular dichroism and birefringence spectra, respectively. Therefore, the chiral interferogram is not a purely even function and it is not symmetric with respect to the zero interferometric position. The circular dichroism and birefringence spectra are retrieved by

taking the imaginary and real part of the FT of the chiral interferogram as shown in equations (37) and (38). The result is shown for the two enantiomers, where the solid lines are referring to the circular dichroism spectra while the dashed lines are the curves corresponding to the circular birefringence spectra. As a comparison, we measured the circular dichroism signals of the two enantiomers of nickel tartrate with a common photo-elastic modulator-based spectropolarimeter [103]. The spectra are shown as colored squares and show a good agreement with the time-domain measurement performed with the interferometer. The commercial spectropolarimeter, used as a reference, could not measure circular birefringence spectra. For this reason, there is no reference plot for the dotted curves in figure 23. This is always the case when a monochromator is used in place of an interferometer as the core element of a spectropolarimeter.

The presented measurement principle employing a CPI is ideal for performing chirality measurement in the infrared and in the visible and ultraviolet spectral ranges. Compared to the available technology, the smaller footprint of the device makes it suitable for space-demanding applications such as inside microscopes. The device can be potentially used for time-resolved optical activity measurements. This can be important to study stereochemical processes [104] such as isomerization, ring-opening, and structural rearrangements in light-driven unidirectional rotary motors [42, 105].

6. Conclusion and outlook

The CPI described in this work is a versatile device that can be used in various experimental setups and scientific fields. It offers several advantages compared to dispersive instruments, mainly thanks to its high throughput, ultra-broadband working range from the visible to the infrared spectral region, and its spectrally flat responsivity. It can be used as enabling technology in several new applications, especially in challenging low-light conditions. For this reason, its commercial version is currently used in hundreds of scientific labs.

In this manuscript, we focused the attention on linear applications in the visible and near-infrared spectral ranges. Indeed, this is the region where the advantages of using a CPI are more relevant. In particular, we described the use of the CPI in measuring EEM maps and how this approach differs from employing a monochromator. We briefly described how this approach can be extended to the SMS field and how the spectral features of chemically equivalent single molecules differ from emitter to emitter. This is a small step forward to the use of a single molecule to sense the nanoscopic environment.

The high light throughput of the CPI is especially beneficial in single-photon counting. In particular, we described how it is possible to measure high-quality TRES maps reaching a picomolar sensitivity level. The CPI is very versatile in this application as it can be used in a broad spectral range from 400 to 2300 nm and the spectral resolution can be varied by simply changing the travel range, without affecting the throughput of the device as with dispersive techniques. Moreover, the beam shape is not altered while passing through the CPI. This

J. Phys. B: At. Mol. Opt. Phys. **54** (2021) 113001

A Perri

helps especially in focusing the light into fiber-coupled detectors such as the recently introduced superconducting nanowire sensors [106].

The advantages of the CPI are maintained by changing the sample from a single point to an extended source. In detail, we described the imaging properties of the interferometer showing its capabilities as the core element of a spectral imager. We described the spectral image of 5 tabulated reflectance standards showing the high accuracy of the measured spectra over a wide spectral range, from 400 to 1000 nm. This is ultimately limited by the used camera and can be extended to the short wave infrared spectral region up to 2300 nm by changing the camera sensor and imaging lens.

Finally, we employed the CPI's sensitivity to the incoming light's polarization state to measure the complete optical activity of a chiral sample, hence both the circular dichroism and birefringence spectra. The application is promising as we dispensed with the use of a photo-elastic modulator and a lock-in acquisition system, greatly simplifying the optical setup with respect to a common spectropolarimeter. This has advantages in terms of cost and compactness that can be beneficial in some industrial applications.

Acknowledgments

Data availability statement

The data that support the findings of this study are available upon reasonable request from the authors.

ORCID iDs

Antonio Perri ⬤ https://orcid.org/0000-0002-1283-8535

References

[1] Fellgett P B 1949 On the ultimate sensitivity and practical performance of radiation detectors *J. Opt. Soc. Am.* **39** 970–6

[2] Jacquinot P 1960 New developments in interference spectroscopy *Rep. Prog. Phys.* **23** 267

[3] Réhault J, Borrego-Varillas R, Oriana A, Manzoni C, Hauri C P, Helbing J and Cerullo G 2017 Fourier transform spectroscopy in the vibrational fingerprint region with a birefringent interferometer *Opt. Express* **25** 4403–13

[4] Preda F, Kumar V, Crisafi F, Figueroa del Valle D G, Cerullo G and Polli D 2016 Broadband pump-probe spectroscopy at 20 MHz modulation frequency *Opt. Lett.* **41** 2970–3

[5] Franceschini P *et al* 2020 Tuning the ultrafast response of Fano resonances in halide perovskite nanoparticles *ACS Nano* **14** 13602–10

[6] Réhault J, Crisafi F, Kumar V, Ciardi G, Marangoni M, Cerullo G and Polli D 2015 Broadband stimulated Raman scattering with Fourier-transform detection *Opt. Express* **23** 25235–46

[7] Kumar V, De la Cadena A, Perri A, Preda F, Coluccelli N, Cerullo G and Polli D 2018 Invited article: complex vibrational susceptibility by interferometric Fourier transform stimulated Raman scattering *APL Photon.* **3** 092403

[8] Brida D, Manzoni C and Cerullo G 2012 Phase-locked pulses for two-dimensional spectroscopy by a birefringent delay line *Opt. Lett.* **37** 3027–9

[9] Borrego-Varillas R, Oriana A, Ganzer L, Trifonov A, Buchvarov I, Manzoni C and Cerullo G 2016 Two-dimensional electronic spectroscopy in the ultraviolet by a birefringent delay line *Opt. Express* **24** 28491–9

[10] Wolz L, Heshmatpour C, Perri A, Polli D, Cerullo G, Finley J J, Thyrhaug E, Hauer J and Stier A V 2020 Time-domain photocurrent spectroscopy based on a common-path birefringent interferometer *Rev. Sci. Instrum.* **91** 123101

[11] Zielnicki K, Garay-Palmett K, Cruz-Delgado D, Cruz-Ramirez H, O'Boyle M F, Fang B, Lorenz V O, U'Ren A B and Kwiat P G 2018 Joint spectral characterization of photon-pair sources *J. Mod. Opt.* **65** 1141–60

[12] Khintchine A 1934 Korrelationstheorie der stationren stochastischen Prozesse *Math. Ann.* **109** 604–15

[13] Wiener N 1930 Generalized harmonic analysis *Acta Math.* **55** 117–258

[14] Griffiths P R and De Haseth J A 2007 *Fourier Transform Infrared Spectrometry* vol 171 (New York: Wiley)

[15] Mooney J and Kambhampati P 2013 Get the basics right: Jacobian conversion of wavelength and energy scales for quantitative analysis of emission spectra *J. Phys. Chem. Lett.* **4** 3316–18

[16] Jablonski A 1933 Efficiency of anti-Stokes fluorescence in dyes *Nature* **131** 839

[17] Kalt H and Klingshirn C F 2019 *Semiconductor Optics 1: Linear Optical Properties of Semiconductors* (Cham: Springer)

[18] Orrit M and Bernard J 1990 Single pentacene molecules detected by fluorescence excitation in ap-terphenyl crystal *Phys. Rev. Lett.* **65** 2716

[19] Cubeddu R, Comelli D, D'Andrea C, Taroni P and Valentini G 2002 Time-resolved fluorescence imaging in biology and medicine *J. Phys. D: Appl. Phys.* **35** R61

[20] Christensen J, Nørgaard L, Bro R and Engelsen S B 2006 Multivariate autofluorescence of intact food systems *Chem. Rev.* **106** 1979–94

[21] Coble P G 1996 Characterization of marine and terrestrial DOM in seawater using excitation–emission matrix spectroscopy *Mar. Chem.* **51** 325–46

[22] Virkler K and Lednev I K 2009 Analysis of body fluids for forensic purposes: from laboratory testing to non-destructive rapid confirmatory identification at a crime scene *Forensic Sci. Int.* **188** 1–17

[23] Comelli D, D'Andrea C, Valentini G, Cubeddu R, Colombo C and Toniolo L 2004 Fluorescence lifetime imaging and spectroscopy as tools for nondestructive analysis of works of art *Appl. Opt.* **43** 2175–83

[24] DeCoster B, Christensen R L, Gebhard R, Lugtenburg J, Farhoosh R and Frank H A 1992 Low-lying electronic states of carotenoids *Biochim. Biophys. Acta* **1102** 107–14

[25] Reilly N J, Schmidt T W and Kable S H 2006 Two-dimensional fluorescence (excitation/emission) spectroscopy as a probe of complex chemical environments *J. Phys. Chem.* A **110** 12355–9

[26] Gascooke J R, Alexander U N and Lawrance W D 2011 Two dimensional laser induced fluorescence spectroscopy: a powerful technique for elucidating rovibronic structure in electronic transitions of polyatomic molecules *J. Chem. Phys.* **134** 184301

[27] Andrade-Eiroa Á, Canle M and Cerdá V 2013 Environmental applications of excitation–emission spectrofluorimetry: an in-depth review I *Appl. Spectrosc. Rev.* **48** 1–49

[28] DaCosta R S, Andersson H and Wilson B C 2003 Molecular fluorescence excitation–emission matrices relevant to tissue spectroscopy *Photochem. Photobiol.* **78** 384–92

[29] Leavesley S J, Walters M, Lopez C, Baker T, Favreau P F, Rich T C, Rider P F and Boudreaux C W 2016 Hyperspectral imaging fluorescence excitation scanning for colon cancer detection *J. Biomed. Opt.* **21** 104003

[30] Ramanujam N 2000 Fluorescence spectroscopy of neoplastic and non-neoplastic tissues *Neoplasia* **2** 89–117

[31] Hirschberg J G, Vereb G, Meyer C K, Kirsch A K, Kohen E and Jovin T M 1998 Interferometric measurement of fluorescence excitation spectra *Appl. Opt.* **37** 1953–7

[32] Anzai H, Joshi N K, Fuyuki M and Wada A 2015 Fourier transform two-dimensional fluorescence excitation spectrometer by using tandem Fabry–Pérot interferometer *Rev. Sci. Instrum.* **86** 014101

[33] Piatkowski L, Gellings E and Van Hulst N F 2016 Broadband single-molecule excitation spectroscopy *Nat. Commun.* **7** 10411

[34] Peng L, Motz J T, Redmond R W, Bouma B E and Tearney G J 2007 Fourier transform emission lifetime spectrometer *Opt. Lett.* **32** 421–3

[35] Perri A, Preda F, D'Andrea C, Thyrhaug E, Cerullo G, Polli D and Hauer J 2017 Excitation–emission Fourier-transform spectroscopy based on a birefringent interferometer *Opt. Express* **25** A483–90

[36] Oriana A, Réhault J, Preda F, Polli D and Cerullo G 2016 Scanning Fourier transform spectrometer in the visible range based on birefringent wedges *J. Opt. Soc. Am.* A **33** 1415–20

[37] Thyrhaug E, Krause S, Perri A, Cerullo G, Polli D, Vosch T and Hauer J 2019 Single-molecule excitation–emission spectroscopy *Proc. Natl Acad. Sci. USA* **116** 4064–9

[38] Schmidt B, Laimgruber S, Zinth W and Gilch P 2003 A broadband Kerr shutter for femtosecond fluorescence spectroscopy *Appl. Phys.* B **76** 809–14

[39] Chen K, Gallaher J K, Barker A J and Hodgkiss J M 2014 Transient grating photoluminescence spectroscopy: an ultrafast method of gating broadband spectra *J. Phys. Chem. Lett.* **5** 1732–7

[40] Shah J 1988 Ultrafast luminescence spectroscopy using sum frequency generation *IEEE J. Quantum Electron.* **24** 276–88

[41] Zhang X-X, Würth C, Zhao L, Resch-Genger U, Ernsting N P and Sajadi M 2011 Femtosecond broadband fluorescence upconversion spectroscopy: improved setup and photometric correction *Rev. Sci. Instrum.* **82** 063108

[42] Conyard J, Addison K, Heisler I A, Cnossen A, Browne W R, Feringa B L and Meech S R 2012 Ultrafast dynamics in the power stroke of a molecular rotary motor *Nat. Chem.* **4** 547

[43] Campillo A and Shapiro S 1983 Picosecond streak camera fluorometry—a review *IEEE J. Quantum Electron.* **19** 585–603

[44] Gobets B, van Stokkum I H M, Rögner M, Kruip J, Schlodder E, Karapetyan N V, Dekker J P and van Grondelle R 2001 Time-resolved fluorescence emission measurements of photosystem: I. Particles of various cyanobacteria: a unified compartmental model *Biophys. J.* **81** 407–24

[45] O'Connor D 2012 *Time-Correlated Single Photon Counting* (New York: Academic)

[46] Becker W 2005 *Advanced Time-Correlated Single Photon Counting Techniques* vol 81 (Berlin: Springer)

[47] Patting M, Wahl M, Kapusta P and Erdmann R 2007 Dead-time effects in TCSPC data analysis Proc. SPIE 6583,

Photon Counting Applications, Quantum Optics, and Quantum Cryptography (11 May 2007) p 658307

[48] Becker W, Bergmann A and Biskup C 2007 Multispectral fluorescence lifetime imaging by TCSPC *Microsc. Res. Tech.* **70** 403–9

[49] Davis S P, Abrams M C and Brault J W 2001 *Fourier Transform Spectrometry* (Amsterdam: Elsevier)

[50] Perri A *et al* 2018 Time- and frequency-resolved fluorescence with a single TCSPC detector via a Fourier-transform approach *Opt. Express* **26** 2270–9

[51] Wolfe W L 1997 *Introduction to Imaging Spectrometers* vol 25 (Bellingham, WA: SPIE Optical Engineering Press)

[52] Eismann M T 2012 *Hyperspectral Remote Sensing* (Bellingham, WA: SPIE Optical Engineering Press)

[53] Grahn H and Geladi P (ed) 2007 *Techniques and Applications of Hyperspectral Image Analysis* (New York: Wiley)

[54] Amigo J M, Babamoradi H and Elcoroaristizabal S 2015 Hyperspectral image analysis. A tutorial *Anal. Chim. Acta* **896** 34–51

[55] Ben-Dor E, Schläpfer D, Plaza A J and Malthus T 2013 Hyperspectral remote sensing *Airborne Measurements for Environmental Research: Methods and Instruments* vol 413 (New York: Wiley) p 456

[56] Sellar R G and Boreman G D 2005 Classification of imaging spectrometers for remote sensing applications *Opt. Eng.* **44** 13602

[57] Lu G and Fei B 2014 Medical hyperspectral imaging: a review *J. Biomed. Opt.* **19** 010901

[58] Dale L M, Thewis A, Boudry C, Rotar I, Dardenne P, Baeten V and Pierna J A F 2013 Hyperspectral imaging applications in agriculture and agro-food product quality and safety control: a review *Appl. Spectrosc. Rev.* **48** 142–59

[59] Huang M, He C, Zhu Q and Qin J 2016 Maize seed variety classification using the integration of spectral and image features combined with feature transformation based on hyperspectral imaging *Appl. Sci.* **6** 183

[60] Mouroulis P, Green R O and Wilson D W 2008 Optical design of a coastal ocean imaging spectrometer *Opt. Express* **16** 9087–96

[61] Scafutto R D P M, de Souza Filho C R and Rivard B 2016 Characterization of mineral substrates impregnated with crude oils using proximal infrared hyperspectral imaging *Remote Sens. Environ.* **179** 116–30

[62] Briottet X *et al* 2006 Military applications of hyperspectral imagery *Targets Backgr. XII Charact. Represent.* **6239** 62390B

[63] Liang H 2012 Advances in multispectral and hyperspectral imaging for archaeology and art conservation *Appl. Phys.* A **106** 309–23

[64] Fischer C and Kakoulli I 2006 Multispectral and hyperspectral imaging technologies in conservation: current research and potential applications *Stud. Conserv.* **51** 3–16

[65] Cucci C, Delaney J K and Picollo M 2016 Reflectance hyperspectral imaging for investigation of works of art: old master paintings and illuminated manuscripts *Acc. Chem. Res.* **49** 2070–9

[66] Gat N 2000 Imaging spectroscopy using tunable filters: a review *Wavelet Appl. VII* **4056** 50–64

[67] Hagen N and Kudenov M W 2013 Review of snapshot spectral imaging technologies *Opt. Eng.* **52** 090901

[68] Fossi A P, Ferrec Y, Roux N, D'almeida O, Guerineau N and Sauer H 2016 Miniature and cooled hyperspectral camera for outdoor surveillance applications in the mid-infrared *Opt. Lett.* **41** 1901–4

[69] Persky M J 1995 A review of spaceborne infrared Fourier transform spectrometers for remote sensing *Rev. Sci. Instrum.* **66** 4763–97

J. Phys. B: At. Mol. Opt. Phys. **54** (2021) 113001

A Perri

[70] Hegyi A and Martini J 2015 Hyperspectral imaging with a liquid crystal polarization interferometer *Opt. Express* **23** 28742–54

[71] August I, Oiknine Y, AbuLeil M, Abdulhalim I and Stern A 2016 Miniature compressive ultra-spectral imaging system utilizing a single liquid crystal phase retarder *Sci. Rep.* **6** 23524

[72] Jullien A, Pascal R, Bortolozzo U, Forget N and Residori S 2017 High-resolution hyperspectral imaging with cascaded liquid crystal cells *Optica* **4** 400–5

[73] Harvey A R and Fletcher-Holmes D W 2004 Birefringent Fourier-transform imaging spectrometer *Opt. Express* **12** 5368–74

[74] Bai C, Li J, Xu Y, Yuan H and Liu J 2018 Compact birefringent interferometer for Fourier transform hyperspectral imaging *Opt. Express* **26** 1703–25

[75] Candeo A, Nogueira de Faria B E, Erreni M, Valentini G, Bassi A, de Paula A M, Cerullo G and Manzoni C 2019 A hyperspectral microscope based on an ultrastable common-path interferometer *APL Photon.* **4** 120802

[76] Krause S and Vosch T 2019 Stokes shift microscopy by excitation and emission imaging *Opt. Express* **27** 8208–20

[77] Born M and Wolf E 2013 *Principles of Optics: Electromagnetic Theory of Propagation, Interference and Diffraction of Light* (Amsterdam: Elsevier)

[78] Saptari V 2004 *Fourier Transform Spectroscopy Instrumentation Engineering* vol 1 (Bellingham, WA: SPIE Optical Engineering Press)

[79] Pelosi C, Lo Monaco A, Bernabei M, Agresti G, Colantonio C, Perri A, Comelli D, Valentini G and Manzoni C 2020 Beyond the visible: the Viterbo Crucifixion panel painting attributed to Michelangelo Buonarroti *Microchem. J.* **154** 104636

[80] Perri A *et al* 2019 Hyperspectral imaging with a TWINS birefringent interferometer *Opt. Express* **27** 15956–67

[81] Berova N, Nakanishi K and Woody R W 2000 *Circular Dichroism: Principles and Applications* (New York: Wiley)

[82] Barron L D 2009 *Molecular Light Scattering and Optical Activity* (Cambridge: Cambridge University Press)

[83] Fasman G D and Dichroism I C 1996 *The Conformational Analysis of Biomolecules* ed G D Fasman (Berlin: Springer)

[84] Sreerama N and Woody R W 2004 Computation and analysis of protein circular dichroism spectra *Methods in Enzymology* vol 383 (Amsterdam: Elsevier) pp 318–51

[85] Hentschel M, Schäferling M, Duan X, Giessen H and Liu N 2017 Chiral plasmonics *Sci. Adv.* **3** e1602735

[86] Helbing J and Bonmarin M 2009 Vibrational circular dichroism signal enhancement using self-heterodyning with elliptically polarized laser pulses *J. Chem. Phys.* **131** 174507

[87] Rhee H, Eom I, Ahn S-H and Cho M 2012 Coherent electric field characterization of molecular chirality in the time domain *Chem. Soc. Rev.* **41** 4457–66

[88] Kramers H A 1927 La diffusion de la lumiere par les atomes *Atti Congr. Int. Fisica* **2** 545–57

[89] Kronig R d L 1926 On the theory of dispersion of x-rays *J. Opt. Soc. Am.* **12** 547–57

[90] Lombardi R A and Nafie L A 2009 Observation and calculation of vibrational circular birefringence: a new form of vibrational optical activity *Chirality* **21** E277–86

[91] Polavarapu P L 1998 *Principles and Applications of Polarization-Division Interferometry* (New York: Wiley)

[92] Ragunathan N, Lee N S, Freedman T B, Nafie L A, Tripp C and Buijs H 1990 Measurement of vibrational circular dichroism using a polarizing Michelson interferometer *Appl. Spectrosc.* **44** 5–7

[93] Polavarapu P L, Deng Z and Chen G-C 1995 Polarization-division interferometry: time-resolved infrared vibrational dichroism spectroscopy *Appl. Spectrosc.* **49** 229–36

[94] Rhee H, June Y-G, Lee J-S, Lee K-K, Ha J-H, Kim Z H, Jeon S-J and Cho M 2009 Femtosecond characterization of vibrational optical activity of chiral molecules *Nature* **458** 310

[95] Rhee H, Choi J-H and Cho M 2010 Infrared optical activity: electric field approaches in time domain *Acc. Chem. Res.* **43** 1527–36

[96] Lepetit L, Chériaux G and Joffre M 1995 Linear techniques of phase measurement by femtosecond spectral interferometry for applications in spectroscopy *J. Opt. Soc. Am.* B **12** 2467–74

[97] Rhee H, Ha J-H, Jeon S-J and Cho M 2008 Femtosecond spectral interferometry of optical activity: theory *J. Chem. Phys.* **129** 094507

[98] Eom I, Ahn S-H, Rhee H and Cho M 2012 Single-shot electronic optical activity interferometry: power and phase fluctuation-free measurement *Phys. Rev. Lett.* **108** 103901

[99] Hiramatsu K and Nagata T 2015 *Communication: Broadband and Ultrasensitive Femtosecond Time-Resolved Circular Dichroism Spectroscopy* (New York: AIP)

[100] Preda F, Perri A, Réhault J, Dutta B, Helbing J, Cerullo G and Polli D 2018 Time-domain measurement of optical activity by an ultrastable common-path interferometer *Opt. Lett.* **43** 1882–5

[101] Jones R C 1941 A new calculus for the treatment of optical Systems I description and discussion of the calculus *J. Opt. Soc. Am.* **31** 488–93

[102] Xie X and Simon J D 1990 Picosecond circular dichroism spectroscopy: a Jones matrix analysis *J. Opt. Soc. Am.* B **7** 1673–84

[103] Castiglioni E, Lebon F, Longhi G and Abbate S 2002 Vibrational circular dichroism in the near infrared: instrumental developments and applications *Enantiomer* **7** 161–73

[104] Meyer-Ilse J, Akimov D and Dietzek B 2013 Recent advances in ultrafast time-resolved chirality measurements: perspective and outlook *Laser Photon. Rev.* **7** 495–505

[105] Strambi A, Durbeej B, Ferré N and Olivucci M 2010 Anabaena sensory rhodopsin is a light-driven unidirectional rotor *Proc. Natl Acad. Sci.* **107** 21322–6

[106] Alonso Calafell I *et al* 2021 Giant enhancement of third-harmonic generation in graphene–metal heterostructures *Nat. Nanotechnol.* **16** 318–24